The long-wavelength admittance and effective elastic thickness of the Canadian Shield

J. F. Kirby[*1] and C. J. Swain[1]

[*] Corresponding author.

[1] Department of Spatial Sciences, Curtin University, Perth, Western Australia, Australia.

Email: j.kirby@curtin.edu.au.

Key Points

1. Wavelet transform can separate convective and flexural signals in the admittance
2. Elastic thickness of Canadian Shield exceeds 80 km

Abstract

The strength of the cratonic lithosphere has been controversial. On the one hand, many estimates of effective elastic thickness (T_e) greatly exceed the crustal thickness, but on the other the great majority of cratonic earthquakes occur in the upper crust. This implies that the seismogenic thickness of cratons is much smaller than T_e, whereas in the ocean basins they are approximately the same, leading to suspicions about the large T_e estimates. One region where such estimates have been questioned is the Canadian Shield, where glacial isostatic adjustment (GIA) and mantle convection are thought to contribute to the long-wavelength undulations of the topography and gravity. To date these have not been included in models used to estimate T_e from topography and gravity which conventionally are based only on loading and flexure. Here we devise a theoretical expression for the free-air (gravity/topography) admittance that includes the effects of GIA and convection as well as flexure and use it to estimate T_e over the Canadian Shield. We use wavelet transforms for estimating the observed admittances, after showing that multitaper estimates, which have hitherto been popular for T_e studies, have poor resolution at the long wavelengths where GIA

and convection predominate, compared to wavelets. Our results suggest that T_e over most of the shield exceeds 80 km, with a higher-T_e core near the south-west shore of Hudson Bay. This means that the lack of mantle earthquakes in this craton is simply due to its high strength compared to the applied stresses.

Index Terms

Lithospheric flexure; Rheology: crust and lithosphere; North America; Spectral analysis; Wavelet transform.

Keywords

Elastic thickness; mantle convection; glacial isostatic adjustment; Canadian shield; wavelet transform; multitaper method.

1. Introduction

The strength of the continental lithosphere (and its depth variation) has important implications in geodynamics [e.g., Chen and Yang, 2004] as it determines the rigidity of the tectonic plates and how they interact and deform, for example, in subduction, orogenesis, and sedimentary basin formation. Two proxies used to characterize lithospheric strength are the effective elastic thickness, T_e, and seismogenic thickness, T_s, which is the maximum focal depth of earthquakes. For the oceans these agree remarkably well [Watts, 2001], implying crust-mantle coupling [Burov and Diament, 1996]. Moreover, they often show similarities in tectonically active regions of continents such as rifts and orogenic belts [e.g., Lowry and Smith, 1995]. However, this relation does not appear to hold for cratons, where T_e estimates span a range from 0 to >120 km, while earthquakes seem to be confined to the crust, mostly the upper crust [Watts, 2001]. This has led some workers to question the reliability of

51 cratonic T_e estimates >25 km [McKenzie and Fairhead, 1997; Maggi et al., 2000; Jackson,
52 2002] and to propose that the cratonic mantle lithosphere is uniformly weak.
53
54 The seismicity of cratons is very low, so it is perhaps not surprising that very few have been
55 found that occur in cratonic mantle. However, a recent paper by Sloan and Jackson [2012]
56 reported earthquakes from the upper mantle, at depths of up to 60 km, beneath the Arafura
57 Sea (just off the coast of the Northern Territory, Australia) in ~150 km thick undisturbed
58 cratonic lithosphere. The authors note that the lower crust in this region is also seismogenic,
59 implying a strong coupled lithosphere, and estimate that 60 km depth is shallower than the
60 600°C isotherm, which is also the isotherm corresponding to the seismogenic thickness of
61 oceanic lithosphere.
62
63 Given the scarcity of earthquakes in the lithosphere of undisturbed cratons, it is natural to try
64 to make reliable T_e estimates to measure its strength. To map T_e variations over North
65 America, we have previously used the admittance between free-air gravity and topography,
66 modeled with a simple thin elastic plate subject to both surface and subsurface loads [Kirby
67 and Swain, 2009]. We have also previously used the Bouguer coherence with Forsyth's
68 [1985] method, and in many cases the two methods gave similar results; however, the latter
69 method may give only upper bounds on T_e if the subsurface loads do not have any
70 topographic expression, which may occur with the erosion that many cratons have suffered
71 [McKenzie, 2003; Kirby and Swain, 2009]. This study employs the free-air admittance.
72
73 McKenzie [2010] pointed out that the gravity and topography of the North American craton
74 are affected at long wavelengths by both glacial isostatic adjustment (GIA) and mantle
75 convection [e.g., Tamisea et al., 2007], and these two processes should be taken into account

when modeling the admittance. In this paper we develop an analytical expression for the admittance of a simple model which combines convection, GIA and flexure and use it to estimate T_e from the free-air admittance over the North American craton calculated using wavelet transforms.

2. Data Analysis

2.1 Wavelet Admittance

The 2-D Morlet-fan wavelet transform [Kirby, 2005] provides estimates of the admittance both locally (at each data grid node) and globally (over the whole data area) [Kirby and Swain, 2004]. The admittance is obtained by taking complete and regular grids of free-air anomaly (g) and topography (h) and computing their fan wavelet transforms, $\tilde{g}$ and $\tilde{h}$, respectively. These are functions of spatial location ($\mathbf{x}$), 2-D Morlet wavelet azimuth (θ), and wavelet scale (s), which may then be simply related to an equivalent Fourier wave number (κ) by the relation $\kappa = |\mathbf{k}_0| / s$, where $|\mathbf{k}_0|$ is the central wave number of the Morlet wavelet [Kirby and Swain, 2011]. The wavelet transforms of the grids were computed using space domain convolution at the largest wavelet scales (longest wavelengths) because Kirby and Swain [2013] found that the faster Fourier transform method produced discretization errors in the representation of the Morlet wavelets at such scales.

The wavelet cross-spectrum between gravity and topography, averaged over azimuth, is formed as

$$S_{gh}^{W}(\kappa,\mathbf{x}) = \left\langle \tilde{g}(\kappa,\mathbf{x},\theta)\ \tilde{h}^{*}(\kappa,\mathbf{x},\theta) \right\rangle_{\theta} \quad (1)$$

and the auto-spectrum of topography as

$$S_{hh}^{W}(\kappa,\mathbf{x}) = \left\langle \tilde{h}(\kappa,\mathbf{x},\theta)\ \tilde{h}^{*}(\kappa,\mathbf{x},\theta) \right\rangle_{\theta} \quad (2)$$

The "local wavelet admittance" is then given by

$$Q(\kappa,\mathbf{x}) = \frac{S_{gh}^{W}(\kappa,\mathbf{x})}{S_{hh}^{W}(\kappa,\mathbf{x})} \tag{3}$$

which is a function of position and wave number. The number of azimuths (i.e., the number of Morlet wavelets comprising a fan) is given by Kirby and Swain [2013], chosen to achieve approximate orthogonality of the wavelets. The "global wavelet admittance" is formed by an additional average, this time over the spatial coordinate:

$$Q(\kappa) = \frac{\left\langle S_{gh}^{W}(\kappa,\mathbf{x})\right\rangle_{\mathbf{x}}}{\left\langle S_{hh}^{W}(\kappa,\mathbf{x})\right\rangle_{\mathbf{x}}} \tag{4}$$

which is a function of wave number only. Here we use several values of the Morlet wavelet central wave number ($|\mathbf{k}_0|$), which affect the resolving power of the wavelets in the space and wave number domains, discussed in section 2.4. We investigated the effect of preprocessing the data prior to wavelet transformation, such as through mirroring and detrending, but found that the resultant admittances were too strongly biased, so did not preprocess.

2.2 Multitaper Admittance

Our multitaper estimates of the admittance were obtained using discrete prolate spheroidal sequences [Slepian, 1978; Thomson, 1982]. We focus on results using $K = 4$ tapers with a half-bandwidth parameter NW = 3, as did McKenzie [2010], though also test other values of K and NW. From here on, we use the notation "[NW, K]-MT" to denote the multitaper method with a half-bandwidth parameter NW and K tapers. The number of tapers is restricted by $K \leq 2\mathrm{NW} - 1$ so as to reduce spectral leakage [Simons et al., 2000, 2003].

The multitaper admittance is computed by averaging the autospectra and cross-spectra of the tapered data over annuli in the wave number domain (with annular-averaged radial wave

number |**k**|) (and which is also, in effect, an azimuthal average) and then over the tapers (τ). If the multitaper cross-spectrum between gravity and topography is

$$S_{gh}^{M}\left(|\mathbf{k}|\right)=\left\langle\left\langle G_{\tau}\left(\mathbf{k}\right)H_{\tau}^{*}\left(\mathbf{k}\right)\right\rangle_{|\mathbf{k}|}\right\rangle_{\tau} \tag{5}$$

and the autospectrum of topography is

$$S_{hh}^{M}\left(|\mathbf{k}|\right)=\left\langle\left\langle H_{\tau}\left(\mathbf{k}\right)H_{\tau}^{*}\left(\mathbf{k}\right)\right\rangle_{|\mathbf{k}|}\right\rangle_{\tau} \tag{6}$$

then the multitaper admittance is

$$Q\left(|\mathbf{k}|\right)=\frac{S_{gh}^{M}\left(|\mathbf{k}|\right)}{S_{hh}^{M}\left(|\mathbf{k}|\right)} \tag{7}$$

where capital letters, *G* and *H*, indicate the Fourier transform of gravity and topography and **k** is the 2-D wave number. The wave number annuli we used had equal spacing in $\log_{10}$ radial wave number. In practice we sum over a half annulus, rather than the full annulus in the wave number domain, because the lower quadrants contain redundant information [e.g., Bracewell, 1986]. As for the wavelet method, we did not preprocess the data prior to application of the multitapers.

Hence, it can be seen that the multitaper admittance is a "global" quantity since it is computed from the entire data set and can therefore be compared directly with the global wavelet admittance. The local wavelet admittance has no multitaper analogue, at least in this study, though it would if small moving windows were to be employed [e.g., Pérez-Gussinyé et al., 2004].

Although both wavelet and multitaper admittances are, in general, complex variables, we invert only the real part since it is less biased by noise [Kirby and Swain, 2009].

146 **2.3 Error Estimates**

147 For both wavelet and multitaper methods, errors on the admittance were computed in two
148 ways, the first being the analytic admittance error formula of Munk and Cartwright [1966]
149 and the second being the jackknife method of error estimation [Thomson and Chave, 1991].

150

151 Munk and Cartwright [1966] and Bendat and Piersol [2000] give the equation for the
152 standard deviation of the admittance as

153 $$\sigma_Q = |Q| \sqrt{\frac{1/\gamma^2 - 1}{2N}} \tag{8}$$

154 where Q is the admittance, N is the number of independent estimates of the admittance, and
155 γ^2 is the coherence. In the wavelet method the coherence is calculated locally (at each grid
156 node) from

157 $$\gamma^2(\kappa, \mathbf{x}) = \frac{\left|S_{gh}^W(\kappa, \mathbf{x})\right|^2}{S_{gg}^W(\kappa, \mathbf{x})\ S_{hh}^W(\kappa, \mathbf{x})} \tag{9}$$

158 and globally (averaged over the entire study area) from

159 $$\gamma^2(\kappa) = \frac{\left|\left\langle S_{gh}^W(\kappa, \mathbf{x})\right\rangle_{\mathbf{x}}\right|^2}{\left\langle S_{gg}^W(\kappa, \mathbf{x})\right\rangle_{\mathbf{x}} \left\langle S_{hh}^W(\kappa, \mathbf{x})\right\rangle_{\mathbf{x}}} \tag{10}$$

160 The multitaper coherence is calculated from

161 $$\gamma^2(|\mathbf{k}|) = \frac{\left|S_{gh}^M(|\mathbf{k}|)\right|^2}{S_{gg}^M(|\mathbf{k}|)\ S_{hh}^M(|\mathbf{k}|)} \tag{11}$$

162 which is a global solution for the entire study area.

163

164 As shown by Kirby and Swain [2009], coherences as given by equations (9)–(11) can
165 sometimes be strongly biased by incoherent signals which manifest in the imaginary parts of

the coherency. They recommended using the squared real coherency (SRC) instead, where the complex coherency is given by, for the wavelet method,

$$\Gamma\left(\kappa,\mathbf{x}\right) = \frac{S_{gh}^{W}\left(\kappa,\mathbf{x}\right)}{\left[S_{gg}^{W}\left(\kappa,\mathbf{x}\right)\ S_{hh}^{W}\left(\kappa,\mathbf{x}\right)\right]^{1/2}} \tag{12}$$

in the local case, by

$$\Gamma\left(\kappa\right) = \frac{\left\langle S_{gh}^{W}\left(\kappa,\mathbf{x}\right)\right\rangle_{\mathbf{x}}}{\left[\left\langle S_{gg}^{W}\left(\kappa,\mathbf{x}\right)\right\rangle_{\mathbf{x}}\left\langle S_{hh}^{W}\left(\kappa,\mathbf{x}\right)\right\rangle_{\mathbf{x}}\right]^{1/2}} \tag{13}$$

in the global case, and by

$$\Gamma\left(\left|\mathbf{k}\right|\right) = \frac{S_{gh}^{M}\left(\left|\mathbf{k}\right|\right)}{\left[S_{gg}^{M}\left(\left|\mathbf{k}\right|\right)\ S_{hh}^{M}\left(\left|\mathbf{k}\right|\right)\right]^{1/2}} \tag{14}$$

for the multitaper method.

The number of independent estimates of the admittance, N in equation (8), is determined as follows. For the local wavelet method we use the number of Morlet wavelets constituting the fan, because Kirby and Swain [2013] demonstrated that they are approximately orthogonal; this value will be the same at all wave numbers. For the global wavelet method we use the product of the number of Morlet wavelets and the number of independent spatial estimates, in a scheme based on the cone of influence of the Morlet wavelet given by Kirby and Swain [2013]; this value will increase with wave number. The cone of influence eliminates wavelet coefficients that might be contaminated by edge effects [e.g., Torrence and Compo, 1998]. For the multitaper method we use the total number of estimates in a half annulus from all tapers, given by the product of the number of tapers (K), and the number of estimates of the autospectrum lying within the half annulus at a given wave number; this value will increase with wave number.

188 The second method we used was the jackknife method [Thomson and Chave, 1991] for
189 wavelets [Kirby and Swain, 2013] and multitapers [Thomson, 2007] except when $K = 1$ in the
190 multitaper method when we used the analytic admittance error formula, equation (8).
191
192 **2.4 Wave Number Resolution**
193 The resolution properties in the wave number domain are controlled by the $|\mathbf{k}_0|$ parameter for
194 Morlet wavelets and the NW parameter for multitapers. Large values of $|\mathbf{k}_0|$ give the Morlet
195 wavelets a high wave number domain resolution but poor space domain resolution, while
196 small values of $|\mathbf{k}_0|$ give a poorer wave number domain resolution but better space domain
197 resolution [Kirby and Swain, 2011, 2013]. The resolution of the Morlet wavelet in the wave
198 number domain was shown by Kirby and Swain [2013] to be given by the half width of the
199 wavelet's Fourier transform at its half amplitude:

200 $$\Delta_{\hat{\psi}}(\kappa) = \kappa \frac{\sqrt{2 \ln 2}}{|\mathbf{k}_0|} \quad (15)$$

201 at an equivalent Fourier wave number κ. It can be seen that the bandwidth varies linearly
202 with wave number, providing good resolution at low wave numbers but poor resolution at
203 high wave numbers.
204
205 For multitapers, small values of NW improve the wave number domain resolution of the
206 spectra, while higher values reduce it [Simons et al., 2000, 2003]. The number of tapers
207 impacts upon resolution too: for a given NW the resolution is improved by using fewer tapers
208 [Simons et al., 2000, 2003]. The bandwidth of the tapers (W) is given by the formula

209 $$W = 2\pi \frac{\mathrm{NW}}{L} \quad (16)$$

210 [Simons et al., 2000; Kirby and Swain, 2013] for W in rad km^{-1}, where L is the length of the
211 data series. For 2-D data we take L to be the geometric mean of the two sides of the

212 rectangular area. Equation (16) shows that, unlike for wavelets, the bandwidth is a constant
213 and does not vary with wave number.
214
215 Performing comparisons between the two methods, Kirby and Swain [2013] found that, at
216 low wave numbers (long wavelengths), the wave number resolution of the wavelet method
217 was considerably better than that of the multitaper method, even when low-$|\mathbf{k}_0|$ wavelets were
218 compared against low-NW tapers. The bandwidth of the two methods (expressed in terms of
219 wavelength rather than wave number) is shown in Figure 1, which clearly shows the superior
220 resolution of the wavelet method at long wavelengths.
221
222 Furthermore, and importantly for this study, Kirby and Swain [2013] found that, again at low
223 wave numbers, spectrum errors for wavelets were smaller than those for multitapers. That is,
224 wavelets with the best wave number resolution deliver the smallest spectrum errors at low
225 wave numbers, whereas tapers with the best wave number resolution deliver the largest
226 spectrum errors at these wave numbers. The sacrifice comes at the high wave numbers, where
227 multitapers outperform wavelets in both wave number resolution and error magnitude.
228
229 **2.5 Inversion**
230 Inversion of the observed admittances was performed using an iterative least squares
231 algorithm [Tarantola, 1987], with the model parameters selected as being those values with
232 the minimum χ^2 misfit between observed and predicted admittances (Q_O and Q_P,
233 respectively). The χ^2 statistic is calculated through

234 $$\chi^2 = \sum_k \left(\frac{Q_O(k) - Q_P(k)}{\sigma_Q(k)} \right)^2 \qquad (17)$$

[e.g., Press et al., 1992], where the summation is over wave number, k, and σ_Q are the observed admittance errors. When inverting for a purely flexural model, the predicted admittance is given by equation (39), and the parameters inverted for are T_e and the loading ratio, f. When inverting for a combined convection-GIA-flexural model (section 4 and Appendix A), the predicted admittance is given by equation (42) and the parameters inverted for are T_e, f, and η (η is the ratio of the GIA and convective topography amplitudes and is described in section 4.1.3 and Appendix A).

Inversions were performed using a thin elastic plate model with a three-layer crust, and internal loading placed at the base of the upper crust. After inversion the loading ratio, f, was converted to an internal load fraction, F, using $F = f/(1+f)$ [McKenzie, 2003]. Errors on the parameters were obtained from the 95% confidence interval contour of the χ^2 misfit surfaces [e.g., Kirby and Swain, 2009].

2.6 Data

Free-air gravity anomaly data were derived from the Earth Gravitational Model 2008 (EGM2008) harmonic geopotential model [Pavlis et al., 2012] expanded to degree and order 1000 (giving an approximate minimum anomaly wavelength of 40 km at the equator) and gridded on a Lambert conic conformal grid with a 20 km grid spacing. Topography data were taken from a harmonic model also provided by the EGM team and also expanded to degree and order 1000. For the admittance analysis and inversion, marine bathymetry was converted to equivalent topography using a rock density of 2800 kg m^{-3}, and a seawater density of 1030 kg m^{-3}.

We performed our analyses over two regions of North America comprising much of the Canadian Shield, shown in Figure 2. Region A is the same as that labeled "box 2" by McKenzie [2010]. Region B was chosen to provide a larger area but without inclusion of oceanic or the Phanerozoic regions of North America. Table 1 shows the values of the densities and depths of the three crustal layers and mantle used in the admittance inversion taken from the CRUST2.0 model [Bassin et al., 2000], together with the values of other required constants.

Note that the wavelet transform is applied to a different sized area than that used in Kirby and Swain [2009], who obtained wavelet coefficients from gravity and topography data given over the whole of the North American continent and surrounding seas, rather than the smaller regions used here (see section 7.1).

3. Admittance of the Canadian Shield – Region A

3.1 Multitaper Results

Figure 3 shows the observed multitaper admittance for region A using several different values of NW and *K*. Comparison between the [3, 4]-MT admittance in Figure 3 and the data from Figure 4f of McKenzie [2010] (who used NW = 3 and $K = 4$), also shown in Figure 3, reveals good agreement in the admittance, given that McKenzie [2010] used free-air anomalies on a 1° grid from a Gravity Recovery and Climate Experiment (GRACE) model (cited in McKenzie [2010]) filtered to pass wavelengths between 500 and 4000 km. We note, however, the difference in error estimates between our version and McKenzie's, with ours being much smaller. McKenzie [2010] did not use equation (8) to calculate his admittance errors but rather used

$$\sigma_Q = 1.96|Q|\sqrt{\frac{1/\gamma^2 - 1}{N/(\mathrm{NW})^2}} \quad (18)$$

Therefore, his errors will be a factor of 2.77 NW times larger than ours computed using equation (8). While it is reasonable to scale the number of independent estimates in an annulus by $(\mathrm{NW})^{-2}$, because of the increase of bandwidth with NW shown in Figure 1, the proper form of this rescaling is not proven, so we do not follow this approach here.

As mentioned, we also computed admittance errors using the jackknife method [Thomson, 2007] when $K > 1$, and Figure 3 shows the errors computed using these two methods. It reveals very similar values, which we take as support for the jackknife approach.

Admittances computed using other values of NW and K are plotted in Figure 3, and the profiles can be seen to have considerably different structures. The profiles with $K = 1$ possess high variability with large error estimates. Interestingly, the change in admittance from [1, 1] to [2, 1] is notable, but the changes between the [2, 1] admittance and that from higher values of NW for $K = 1$ are slight. Indeed, Figure 3 shows that the largest changes in admittance result from an increase of the number of tapers, rather than from changes in NW. From the discussion in section 2.4 we know that the wave number resolution worsens with the use of more tapers at a given NW [Simons et al., 2000, 2003]. This is shown in Figure 3 by the flattening of the admittance at long to middle wavelengths as the spectral information is smeared over increasing bandwidth.

It is also known that higher values of K improve the estimation variance of the power spectra [Simons et al., 2000, 2003], demonstrated in Figure 3 by a decrease of the errors with increasing K.

We therefore conclude that no particular values of NW or *K* can be deemed to be favored. The difference between the [1, 1] and [7, 13] admittances in Figure 3 is striking and could be inferred to describe completely different tectonic regimes.

3.2 Wavelet Results

Figure 4 shows the global wavelet admittance for region A. An e^{-1} cone of influence [Kirby and Swain, 2013] was applied to the autospectra and cross-spectra before spatial averaging to remove edge effects. While Figure 4 shows results from the $|\mathbf{k}_0| = 3.081$ wavelet, we do not place high importance upon them because low-$|\mathbf{k}_0|$ wavelets have a comparatively poor wave number resolution (section 2.4), giving somewhat "smeared" profiles in this domain, an effect seen clearly in Figure 4. In contrast to the multitaper results, the profiles in Figure 4 exhibit a reasonable degree of similarity at long wavelengths (>700 km). At the longest wavelengths (>1500 km approximately) the profiles possess admittances within a range of ~60–70 mGal/km. As wavelength decreases, so does the admittance which falls to values of 20–40 mGal/km at approximately 1000–1200 km wavelength. At shorter wavelengths still (700–1000 km) the admittance rises again to >100 mGal/km. The importance of these features (a large long-wavelength admittance, dropping to low values as wavelength decreases, and rising again) will be discussed in section 4.

We also note the decrease in error with increasing $|\mathbf{k}_0|$ at long wavelengths, as described in section 2.4 and Kirby and Swain [2013], particularly for the jackknife method. At many wavelengths the analytic errors are larger than the jackknifed estimates, though this is not seen in region B, where the two methods give very similar errors.

Note that the wavelet method gives more estimates at the long wavelengths than the multitaper method. With multitapers, spectral estimates are computed at the discrete nodes of a wave number domain grid, as required by the fast Fourier transform. Thus, the first harmonic occurs at the "Rayleigh wave number," being $2\pi/(N_x\Delta x)$ for the x wave number, with successive harmonics being integer multiples of this. In addition, the annular averaging of the autospectra and cross-spectra necessitates the averaging of the first few harmonics, resulting in the first spectral estimate being displaced to higher wave numbers than the Rayleigh wave number.

In contrast, the wavelet coefficients are obtained by space domain convolution of a scaled wavelet with the data [Kirby and Swain, 2013]. With the continuous wavelet transform there are few restrictions placed upon the value of the scales [e.g., Lee, 1996; Torrence and Compo, 1998; Antoine et al., 2004], though here we stipulate that the largest scale is assigned an equivalent Fourier wave number equal to the largest of the two Rayleigh wave numbers in the x and y directions, while the smallest scale has an equivalent Fourier wave number equal to the Nyquist wave number. Our choice of scales is described in Kirby and Swain [2013], though here we use eight voices (i.e., eight scales per octave, with one octave being a doubling of wave number). Thus, the comparatively large number of long-wavelength estimates is a result of convolving the data with many large-scale wavelets.

Note that, although Morlet wavelets are nonorthogonal and so cause energy leakage between harmonics, the number of voices chosen does not increase or reduce leakage per se. That is, choosing two or four voices would give fewer estimates in plots like Figure 4, but common estimates would still have the same admittance value. Larger values of voice merely increase

redundancy but also make the wavelet frame tighter which means that less energy is lost upon wavelet transformation [Lee, 1996].

3.3 Comparison and Interpretation

According to models describing the flexure of a thin, elastic plate, the free-air admittance at very long wavelengths tends to zero, reflecting the isostatic compensation of such large loads. However, Figures 3 and 4 show that the longest wavelength admittance values range between ~60 and 75 mGal/km in both the multitaper and wavelet results for region A, for any [NW, K] or $|\mathbf{k}_0|$ values. The K = 1 multitaper admittance profiles then decrease as wavelength decreases, markedly for the NW = 1 result and not so much for higher values of NW, though given the error bars and poor bandwidth resolution of the multitaper method at long wavelengths, this observation should be treated with caution. Admittances from the higher values of NW and K show very little change in the long-wavelength admittance. The wavelet admittance, on the other hand, exhibits a pronounced minimum at wavelengths of approximately 1200–800 km, depending upon $|\mathbf{k}_0|$. For the 7.547 profile in Figure 4, the admittance low occurs at a wavelength of 1177 km, while the width of the dip extends from 908 to 1527 km wavelength. From equation (15), the 7.547 wavelet resolution at 1177 km wavelength is from 1017 to 1394 km, well within the dip extents. In contrast, the [3, 4]-MT resolution at this wavelength is from 462 to >10,000 km, from equation (16) with L = 2280 km. Therefore, if an admittance dip is actually present, and not an artifact, the wavelet method would resolve it, while the [3, 4]-MT method would not.

As mentioned, McKenzie [2010] invoked a model describing the combined effects of mantle convection and glacial isostatic adjustment (GIA) in order to explain the large free-air admittance at long wavelengths. In the following section we explore the possibility that a dip

381 in the admittance as seen in the wavelet results could also be explained by convection and
382 GIA.
383
384 **4. Models of Mantle Convection, Flexure, and GIA**
385 **4.1 Synthetic Model Generation**
386 In order to test the resolution and accuracy properties of the various wavelet and multitaper
387 methods, when attempting to recover the admittance in the presence of flexure, mantle
388 convection, and GIA, we applied the analysis methods to synthetic data of known parameters
389 (as was done by Macario et al. [1995] to test the coherence method). That is, we generated
390 100 synthetic models of gravity and topography arising from flexural, GIA, and mantle
391 convection processes and determined the admittance from the combined gravity and
392 topography using the wavelet and multitaper methods. For all our synthetic surfaces we used
393 fractal models of dimensions 5100×5100 km generated using the SpectralSynthesisFM2D
394 algorithm of Saupe [1988]. Two hundred different values of the random fractal seed thus give
395 100 different fractal surface pairs.
396
397 **4.1.1 Mantle Convection**
398 Synthetic grids of the gravity and topography due to mantle convection, $g_C(\mathbf{x})$ and $h_C(\mathbf{x})$,
399 respectively, were generated as follows. We first generated a random fractal surface of fractal
400 dimension 2.0 and maximum amplitude of T_0 = 100°C [McKenzie, 2010], representing a
401 temperature distribution, $t(\mathbf{x})$. We then took its Fourier transform and used equations (26) and
402 (28) to generate the Fourier transforms of the gravity and topography, then inverse Fourier
403 transformed both back to the space domain (see section A1). The temperature distribution
404 was assigned a depth a = 220 km below the Earth's surface. We used two uniform-T_e plates,
405 with T_e = 30 and 150 km.

406

407 **4.1.2 Flexure**

408 To generate the flexural free-air anomaly, $g_F(\mathbf{x})$, and topography, $h_F(\mathbf{x})$, we first created pairs
409 of random fractal surfaces (fractal dimension 2.5) and used these as the two initial loads on a
410 plate of known, uniform T_e. The flexure equation was then implemented in the Fourier
411 domain using equation (33) to give the postflexure gravity and topography, followed by
412 inverse Fourier transformation back to the space domain. Crust and mantle densities and
413 depths were chosen to be the same as those from the Canadian Shield region A (Table 1). The
414 postflexural topography was rescaled to have the same variance as the convective
415 topography, and the postflexural free-air anomaly adjusted by the same factor for
416 consistency. We used two uniform-T_e plates, with T_e = 30 and 150 km and both with uniform
417 (wave number-independent) F = 0.5 (f = 1).

418

419 **4.1.3 GIA**

420 The GIA topography is generated in the following manner. We first generated a random
421 fractal surface, $h(\mathbf{x})$, in the space domain of fractal dimension 2.0 and rescaled it to have the
422 same variance as the convective topography. We then used the equation

423 $$h_G = R_{CG} h_C + \sqrt{1 - R_{CG}^2}\, h \qquad (19)$$

424 [Macario et al., 1995] to generate a new surface, $h_G(\mathbf{x})$, the topography due to GIA. The new
425 surface is potentially correlated with the convective topography by the parameter R_{CG}, the
426 assigned correlation coefficient; we used values of R_{CG} = 0 (uncorrelated) and 1 (correlated).
427 The GIA topography surface was then reassigned the same variance as the convective
428 topography and multiplied by a constant η, for the following reason.

429

430 In our analyses we assume that the convective and GIA topography signals are in phase, i.e.,

$$\frac{H_G}{H_C} = \eta \tag{20}$$

where η is a constant at all wave numbers and represents the ratio between the spectrum amplitudes of the GIA and convective topographies (see section A4). This assumption, also made by McKenzie [2010], was made to simplify the equation for the combined admittance from flexure, convection, and GIA processes (section A4). It reflects the fact that, at least in North America and at very long wavelengths, the ice sheet is thought to have covered an area approximately coincident with the large geoid low over the Canadian Shield [Tamisiea et al., 2007; McKenzie, 2010].

Hence, setting $R_{CG} = 1$ in equation (19) and multiplying the resulting surface by η will ensure that equation (20) is met at all wave numbers, since h_C and h_G will be essentially the same surfaces. When $R_{CG} < 1$, however, it is uncertain what will be the relationship between the Fourier transforms of the convective and GIA topographies; certainly η would be wave number dependent, and probably complex valued. Nevertheless, by rescaling the variance of h_G so that $\text{var}[h_G(\mathbf{x})] = \eta^2 \text{var}[h_C(\mathbf{x})]$, we at least make some attempt at satisfying equation (20).

When generating our synthetic models, we set $\eta = 0.5$. The GIA gravity is then generated in the Fourier domain from the formula $G_G = Q_G H_G$, where Q_G is given by equation (31). The GIA gravity transform was then inverse transformed back to the space domain.

4.1.4 Combined Fields

The total combined gravity is then $g(\mathbf{x}) = g_C(\mathbf{x}) + g_G(\mathbf{x}) + g_F(\mathbf{x})$, and the total combined topography is $h(\mathbf{x}) = h_C(\mathbf{x}) + h_G(\mathbf{x}) + h_F(\mathbf{x})$.

455

456 **4.2 Synthetic Model Analysis**

457 Once the 100 synthetic models had been generated, we then computed the observed
458 admittance between (1) the synthetic flexural gravity and topography grids and (2) the
459 synthetic combined gravity and topography grids, for each of the 100 models and for each T_e
460 plate. We used the wavelet method with $|\mathbf{k}_0|$ = 3.773 and 7.547 and both [1, 1]-MT and [3, 4]-
461 MT methods. The 100 admittances of each T_e were then averaged and are presented (for the
462 periodic data) in Figure 5. The inversion of the single, averaged admittance for a model,
463 against a theoretical prediction, is discussed in section 4.3.

464

465 Turning to the flexural-only models first, Figure 5a shows that the 7.547-WT, [1, 1]-MT, and
466 [3, 4]-MT admittances follow the theoretical curve very well when T_e is low, but the 3.773-
467 WT admittance sees the transition wavelength pushed to slightly smaller wavelengths due to
468 the poor wave number resolution of this wavelet at short wavelengths. Here the admittance
469 transition occurs at short wavelengths because T_e is relatively low. When T_e is high, however,
470 the transition is at long wavelengths (Figure 5b) and only the 7.547-WT and [1, 1]-MT
471 methods have success at recovering the true admittance. The 3.773-WT and [3, 4]-MT
472 admittances would yield an underestimated T_e upon inversion (see Table 2).

473

474 Concerning the combined models with correlated convective and GIA topographies (R_{CG} = 1)
475 (Figures 5c and 5d), the theoretical profiles show a dip in the admittance separating the long-
476 wavelength high of the convective admittance and the shorter-wavelength high of the flexural
477 admittance. This dip, seen in the North American wavelet admittances (Figure 4), is predicted
478 by the theory presented in Appendix A. That is, the convective and flexural regimes are
479 distinguishable, even for high-T_e plates, and they are separated at the wavelength at which the

observed admittance has a minimum: above this wavelength, convection and GIA effects dominate; below it, flexural effects dominate. The long wavelength combined admittance value is governed by the relative contributions of the convective and GIA processes. As shown in section A1 and A2 the very long-wavelength mantle and GIA admittances have asymptotic values of approximately 48 and 143 mGal/km, respectively; when both processes are present the combined long-wavelength admittance value will lie between these, according to our model, with the actual value depending upon η, the GIA-convection topography ratio (section 4.1.3).

The 7.547-WT, 3.773-WT and [1, 1]-MT admittances agree well for the lower-T_e plate (Figure 5c) and fairly well for the high-T_e plate (Figure 5d), though as in the flexure-only case the 3.773-WT admittance does not properly resolve the flexural transition at low T_e owing to its poorer wave number resolution at short wavelengths. The [3, 4]-MT method, however, gives a very poor match to the predicted admittance with both high- and low-T_e plates. While the flexural transition is well matched in the 30 km plate, the long-wavelength signal due to convection is not. For the T_e = 150 km plate, the [3, 4]-MT admittance behaves even more badly. The long-wavelength admittance plateaus at a constant value well into the shorter-wavelength harmonics, and the dip magnitude is much underestimated.

Note that we would expect the multitaper methods to perform better on our synthetic models than on the North American region A. This is because the models cover a larger area (5100×5100 km as opposed to 2600×2000 km), and so by equation (16) the tapers will have a better wave number resolution. Despite this fact, the [3, 4]-MT method still does not perform well with the synthetic models.

When there is no forced correlation between convective and GIA topographies (R_{CG} = 0) (Figures 5e and 5f), the 7.547-WT, 3.773-WT, and [1, 1]-MT methods still out-perform the [3, 4]-MT method but with reduced impact. The dip is still resolved with these three methods but is broader and shallower. The [3, 4]-MT method with high T_e almost completely fails to resolve the dip.

The results from nonperiodic data were very similar to those for periodic data. This was also found for power spectra by Kirby and Swain [2013] and is due to the application of a cone of influence to the nonperiodic data with wavelets and the tapering action of the multitapers. With nonperiodic data, the relationships between method results were the same as for periodic data, that is, the 7.547-WT, 3.773-WT, and [1, 1]-MT methods still out-perform the [3, 4]-MT method. This observation was most apparent when R_{CG} = 1 but less so when R_{CG} = 0. We found that the 7.547-WT long-wavelength admittance had slightly higher variance with the nonperiodic data.

4.3 Synthetic Model Inversion for T_e

We inverted averaged observed synthetic admittances using the procedure outlined in section 2.5. We will most often represent η in terms of the parameter η', where

$$\eta' = \frac{\eta}{1+\eta} \tag{21}$$

which has values constrained between 0 and 1, rather than 0 and ∞. The parameter η' can be thought of as the fraction of the joint convective-GIA topography due to GIA. If required, η can be obtained from η' using $\eta = \eta'/(1-\eta')$. So the assigned model value of η = 0.5 gives η' = 0.33.

As discussed in section A4, evaluation of equation (42) (the combined admittance) requires knowledge or assumption of the flexural topography and temperature amplitude spectra. These were estimated from their power spectra, through computation of the fan wavelet transform of the space domain grids of flexural topography and temperature [Kirby and Swain, 2013]. This gave amplitude spectra of $H_F(k) = 3.2\times10^{-6}\, k^{-1.5}$ and $T(k) = 2.7\times10^{-10}\, k^{-2}$ for wave number k in rad m^{-1}, temperature in °C, and topography in meters (see section A4).

Table 2 shows the recovered T_e, F, and η' values from the inversions of admittances from periodic data. In general, T_e values are consistently underestimated by all methods, though the true T_e is sometimes within the 95% confidence limits. Forcing correlation between convective and GIA topographies in the models ($R_{CG} = 1$) improves the estimation of the parameters, as expected, but we note that using nonperiodic data did not make much difference. Values of F and η' are generally recovered fairly well.

We also explored the effect of wrongly estimating the topography amplitude spectrum, A_F, during inversions. With results discussed in section A4, we found that the errors in the parameters increase with increasing model T_e and that the parameter η' is much more sensitive to variations in A_F than are T_e and F.

5. Summary

So far, our studies have shown the following:

1. Observed Canadian Shield admittances show a low-admittance dip separating high values of admittance at longer and shorter wavelengths. This is most apparent in the wavelet results, but only just with the [1, 1]-MT method, and not at all in the other multitaper results (Figures 3 and 4).

2. A model of combined convective, GIA, and flexural processes produces a similar admittance dip separating the flexural from convective/GIA regimes (Figure A1).
3. Wavelet and multitaper analyses of synthetic models generated from convective, GIA, and flexural processes yield observed admittances that correctly resolve the dip, except when the [3, 4]-MT method is used (Figure 5). Tapers with these parameters do not have sufficient wave number resolution to accurately resolve the dip.

In subsequent sections we estimate T_e for the Canadian Shield using our combined convection-GIA-flexure model and WT admittances with $|\mathbf{k}_0|$ = 5.336 and 7.547.

6. Elastic Thickness of the Canadian Shield

6.1 Global Admittance

6.1.1 Region A

Figure 6 shows the results of inverting two global wavelet admittance profiles ($|\mathbf{k}_0|$ = 7.547 and 5.336) for the parameters T_e, F, and η' for region A, while Table 3 also shows their error bounds. The wavelet results are consistent, with approximate values of T_e at 155 km, F at 0.5, and η' at 0.3. We used the inversion procedures outlined in section 2.5. We estimated the fractal topography parameters of equation (43) by comparison of the square of that equation with the global wavelet power spectrum of the topography for region A; this gave A_F = 2.7×10^{-6}, and ζ_F = 1.5 (FD = 2.5). For the temperature amplitude spectrum, we assumed a fractal dimension of 2, giving ζ_T = 2, and then adjusted A_T so that the temperature at the longest wavelength in the data was 100°C: this gave $A_T = 8.0\times10^{-10}$. We also assumed a lithosphere thickness (a) of 220 km. In his computations, McKenzie [2010] took a = 120 km, but it is clear from his Figure 3a that the lithosphere of the Canadian Shield is much thicker than this value.

6.1.2 Region B

When the larger region (B) is considered, the best fitting parameter values (Figure 7 and Table 3) are somewhat different, especially for η'. It could be reasoned that the extent of this box includes geological provinces of different composition, rheology, and loading regimes that are not present in region A, and also areas that were less loaded during the last glacial maximum, and are less affected by mantle convection (which produces the geoid low over Hudson Bay).

The above observations imply that analyses of global admittances could give erroneous results, since the gravity and topography spectra may be considerably nonstationary. That is, inversions of global admittances, where a single admittance profile is obtained for the whole grid (given a cone of influence), may give parameter estimates that are not representative of the whole area. To allow for this, we next study the local admittances.

6.2 Local Admittance

6.2.1 Region A

Rather than computing the admittance at each of the 20×20 km grid nodes, we spatially averaged the autospectra and cross-spectra over 32×32 grid nodes, giving a 640×640 km spatially averaged admittance. The spatial averaging procedure is similar to that given in equation (4), except that the averaging is not global. The spatially averaged observed admittances and their errors are shown as black curves in Figure 8. We used wavelets with a $|\mathbf{k}_0|$ of 5.336, since this has a good resolution in the wave number domain and a reasonably good resolution in the space domain. We did not apply a cone of influence in this case, which

603 we justify by noting that the long-wavelength admittances when using a wavelet with high
604 spatial resolution ($|\mathbf{k}_0| = 2.668$) are reasonably stationary over the area.
605
606 Inversions for T_e, F, and η' were performed on the spatially averaged observed admittances,
607 over wavelengths >500 km. We only inverted the midwavelength to long-wavelength
608 portions because the short-wavelength admittance values in Figure 8 are sometimes much
609 lower (and more variable) than theory predicts. The reason for this is that wavelets have a
610 good spatial resolution (and poor wave number resolution) at short wavelengths, and since
611 the short-wavelength admittance is strongly dependent upon the upper crust density, any
612 lateral density variations would be picked up well by the wavelets. We also note that the error
613 bars are larger at the short wavelengths. The best fitting predicted admittances and T_e values
614 are also shown in Figure 8. It can be seen that the long-wavelength admittance in all 640×640
615 km grid cells is consistently nonzero, and exhibits the dip separating convective/GIA
616 processes from the flexural signature. With the exception of the lower left cell where the
617 observed admittance has low values at middle to short wavelengths and the inversion is
618 ambiguous, T_e is high, ranging from ~60 to 160 km, with its largest value at the southwest
619 corner of Hudson Bay.
620
621 **6.2.2 Region B**
622 A similar plot is shown in Figure 9, for region B. Again, larger T_e values are exhibited around
623 the southwest of Hudson Bay, where the inversions are all very representative of the observed
624 admittances. To the north and west of the region, T_e is low, but we note that the observed
625 admittances have very low values at all wavelengths, rendering the inversions unreliable.
626 Though the absolute T_e values differ somewhat, the T_e structure of regions A and B is similar,
627 with a high-T_e core around the southwest of Hudson Bay, between this and Lake Winnipeg.

Finally, and for visual clarity, Figure 10 shows an interpolated T_e map for region B, derived from Figure 9. In Figure 10 the region of T_e > 80 km extends throughout most of the shield and part of the eastern Interior Platform adjacent to the Superior and Churchill provinces. To the south and east, this high-T_e zone approximately follows the southern boundary of the Superior province, while to the north the zone does not extend into the Arctic platform. We note that the Slave and Bear provinces possess lower T_e values, in the range 40–50 km approximately.

7. Discussion

7.1 T_e of the Canadian Shield

The results of the synthetic modeling suggest that the observed global wavelet admittance of the Canadian Shield is representative of the true admittance of the shield as a whole. The prominent long-wavelength dip in the Canadian Shield wavelet admittance (Figures 6 and 7) is explained by theoretical and synthetic models of convection, GIA, and flexure, and by the good wave number resolution of the (large $|\mathbf{k}_0|$) fan wavelet method. And despite its high variance, the [1, 1]-MT admittance results in Figure 3 reveal the dip as well. Together, including the spatial distribution of T_e from the local admittance analyses, these observations suggest that the elastic thickness of the majority of the Canadian Shield exceeds 80 km, with a higher-T_e core located to the immediate southwest of Hudson Bay. Even if our theoretical admittance model is in error − and from the study in section A4 the errors are most likely to lie in the assumption of coherent convective and GIA topography and in the estimation of flexural topography power − the shape and location of the observed dip in the admittance are indicative of high elastic thickness.

Kirby and Swain [2009] also created a T_e map of North America using the method of McKenzie and Fairhead [1997], from the inversion of the free-air admittance, assuming uniform *f*, and with loading of a three-layer crust at the base of the upper crust. However, they used a flexural-only model, and their Figure 15d shows a high-T_e core that is further north than the one we have generated here using the convection/GIA/flexure model, over the northwest coast of Hudson Bay.

As mentioned in section 2.6, Kirby and Swain [2009] used data over the whole of the continent and surrounding seas, shown in their Figure 12. With such a large area (6000×8640 km), the wavelets at the largest scales have very poor spatial resolution, which results in them capturing the very long wavelength continental/bathymetric signal in which Airy isostasy dominates, resulting in long-wavelength free-air admittances of approximately 0. This is seen in Figure 11, which shows a comparison of admittances covering the same area over Hudson Bay: the black curves are from this study; the red curves were computed from the same data set (EGM2008) covering the whole continent, as in Kirby and Swain [2009]. Only when a smaller region is analyzed, as in this study, does the convection/GIA signal cease to be dominated by the isostatic signal, and becomes apparent. To a certain extent, this reduces the usefulness of the wavelet transform in obtaining admittances or coherences over very large areas or even whole planets; a region-by-region analysis is sometimes still required.

The high T_e over the shield is corroborated in several earlier studies of the region, and all of the following have used Forsyth's Bouguer coherence method. Bechtel et al. [1990] and Pilkington [1991] estimated T_e in moving windows using the periodogram method of spectral estimation, locating a core of T_e > 120 km to the immediate south of Hudson Bay. Later, Wang and Mareschal [1999] used maximum entropy spectral estimation to produce a high-

678 resolution T_e map, with the core (T_e > 100 km) located in a similar region to ours, to the
679 Bay's south-west. The spatial distribution of T_e within the maps of Audet and Mareschal
680 [2004a, 2004b], however, is somewhat different from ours, though their values do exceed 100
681 km in places (e.g., over Hudson Bay); they used maximum entropy and multitapers. Wavelets
682 were also used by Audet and Mareschal [2007] to estimate a T_e map over the Canadian
683 Shield. Their map shows more similarities with ours, though while it is difficult to tell exactly
684 where their high-T_e core lies, it is certainly to the south and/or west of Hudson Bay. Kirby
685 and Swain [2009] used wavelets with Forsyth's method to reveal the T_e > 100 km core
686 extending northwest from the center of the Bay. They also used a technique to detect noise in
687 Bouguer coherence data (section 7.3) so that estimates affected by it could be screened out.
688 This study showed that although coherence estimates over parts of the North American
689 Craton in the U.S. are affected by noise, those for most of the Canadian Craton are not.
690 Finally, in an early study, Stephenson and Beaumont [1980] analyzed anisotropy in the
691 admittance over the shield with a view to detection of preferential directions in upper mantle
692 small-scale convection. While they claimed to have found evidence for this, they did not
693 estimate T_e.
694
695 McKenzie and Fairhead [1997] and McKenzie [2003] made no estimates of T_e over the
696 Canadian Shield, though the latter did make some over the Midcontinent Rift by modeling
697 gravity profiles, reporting values of 9 and 22 km, which agree with our result for the SW
698 corner of region B (Figure 9).
699
700 Using data from an area identical to our region A, McKenzie [2010] calculated the free-air
701 admittance using [3, 4] multitapers (as noted in section 3.1 above) with results shown in
702 Figure 3. He fitted the medium-short wavelength (150–500 km) admittance with a flexure-

703 only model, obtaining a T_e of 29 km. His model did not include convection and GIA, and
704 moreover, as we have shown above, these multitaper admittances are unlikely to represent the
705 true admittance behavior of the shield at longer wavelengths.
706
707 **7.2 Temperature and Other Controls of Continental T_e**
708 Our high-T_e estimates for the Canadian Shield imply that (a) a substantial fraction of its long-
709 term lithospheric strength resides in the mantle; (b) the uppermost mantle and lowermost
710 crust are probably mechanically coupled [Burov and Diament, 1996]; and (c) the lower crust
711 and upper mantle temperatures are relatively low. An additional possible implication is that
712 (d) both lower crust and upper mantle are relatively anhydrous, as it has long been held [e.g.,
713 Li et al., 2008] that small amounts of water in the minerals that they contain (e.g., olivine and
714 pyroxene) may reduce their viscosity significantly.
715
716 **7.2.1 Temperature**
717 As noted earlier, the 600°C isotherm often gives a reasonable approximation for T_e in oceanic
718 lithosphere. However, in relation to the continental lithosphere, Burov and Diament [1995]
719 quote critical temperatures for long-term ductile flow in olivine of 600–700°C based on
720 laboratory data scaled to real-Earth values at geological time scales and "rheologically
721 significant" strain rates. They further suggest that the base of the mechanical lithosphere, for
722 small applied stresses, corresponds to the 700–800°C isotherm. Geotherms computed by
723 Griffin et al. [2004] from analyses of garnets from xenocrysts brought up by kimberlite
724 eruptions at two locations within the Canadian Shield, to the west of James Bay, indicate that
725 the temperatures at 80 km and 120 km depth are approximately 550°C and 750°C,
726 respectively. These low geotherms are supported by new heat flow data and geotherm
727 modeling (incorporating shear velocity data from seismic tomography) presented in Lévy et

al. [2010, Figure 14] for their data window "I" just east of James Bay. This suggests a cooler lithosphere near the center of the shield than the study of Kopylova et al. [1999], which determined a temperature of 740°C at 100 km depth in the Slave craton. The Slave, of course, is at the periphery of the shield and might therefore be expected to be warmer, an observation supported by our T_e estimate there (<50 km).

7.2.2 Crust/Mantle Coupling

The lower crustal mineralogy is typically ductile at a considerably lower temperature than for olivine, so it will more likely be coupled to the upper mantle if the crust is relatively thin. Burov and Diament [1996] suggest a critical thickness of 35 ± 5 km, but this obviously depends on the geotherm, which the previous paragraph indicates is very low. Crustal seismic studies reveal that the crust has a uniform thickness of 38 ± 1 km around the periphery of Hudson Bay [Pawlak et al., 2011], with thinning under the Hudson Bay basin of 3 km.

7.2.3 Water

The strength of olivine is likely to control the rheology of the cratonic upper mantle because it makes up >50% of a typical mantle peridotite and its strength is less than that of pyroxenes [Peslier et al., 2010]. The increase of mantle viscosity with decrease of the water content of olivine has often been proposed to account for the strength of the cratonic mantle [e.g., Pollack, 1986]. Peslier et al. [2010] measured the water content of a number of olivine samples in xenoliths brought to the surface from depths of 80–200 km by kimberlite eruptions on the Kaapvaal Craton, South Africa. Their main result was that the water content decreased dramatically from ~75 ppm to <10 ppm just above the inferred lithosphere-asthenosphere boundary, providing an explanation for why cratons are resistant to delamination by asthenospheric flow. However, their graph of water content versus pressure

753 also shows a drop of similar magnitude between 110 and 80 km depth, implying that the
754 mantle is anhydrous at the latter depth. Our T_e data suggest that similar results would be
755 obtained for xenoliths from the Canadian Shield. This conclusion hinges on the assumption
756 that such small water contents reduce the viscosity of olivine significantly, which has been
757 generally accepted up to now but was recently challenged by Fei et al. [2013], who found that
758 the effect of water on the rheology of olivine may have been overstated in earlier studies and
759 is probably not significant. However, as Brodholt [2013] notes, further studies are required to
760 repeat and extend their work before we can be confident in this new discovery.
761
762 **7.3 Noise**
763 McKenzie and Fairhead [1997] and McKenzie [2003, 2010] raised the issue that noise would
764 affect T_e estimates obtained from the Bouguer coherence method of Forsyth [1985]. They
765 proposed that, since the admittance was less prone to bias by gravitational noise (being that
766 part of the gravity field uncorrelated with the topography), this measure would reveal more
767 reliable T_e estimates. They also proposed that neither method could recover meaningful T_e
768 estimates unless the free-air coherence had values close to unity at short wavelengths.
769 However, Kirby and Swain [2009] demonstrated that the free-air coherence was not a good
770 indicator of noise and instead the imaginary part of the observed free-air coherency contained
771 the information that would identify the harmonics at which noise biased the Bouguer
772 coherence. They also recommended use of the imaginary part of the free-air admittance when
773 identifying noise that could potentially bias inversion of the real admittance.
774
775 Here we revisit the noise issue. A synthetic modeling experiment is detailed in Appendix B
776 and shows that at noise levels where the free-air and Bouguer coherences (SRCs) are greatly
777 affected, the free-air admittance is not and would still be invertible for reasonably accurate T_e

778 values. The imaginary part of the free-air coherency, however, remains of paramount
779 importance at identifying coherence-biasing noise when inverting the Bouguer coherence.
780
781 Figures 8, 9, and 11 show the imaginary component of the free-air admittance (Q_I) at
782 locations within the study area. Although the imaginary component sometimes reaches high
783 values (>50 mGal/km), it does not do so at wavelengths close to the real admittance (Q_R)
784 transition and almost never at the long wavelengths where the dip between convective and
785 flexural signals occurs. We believe now that the interpretation of admittance-biasing noise in
786 Kirby and Swain [2009] was unduly pessimistic. The greater scale density of eight voices
787 (scales per octave) used here, versus the four used in Kirby and Swain [2009], allows a more
788 precise estimate of both the Q_R transition wavelength and the wavelengths at which Q_I
789 reaches high absolute values. Our new estimates of Q_I in Figures 8 and 9 hence show that Q_I-
790 implied noise hardly affects estimation of the Q_R transition in eastern Canada.
791
792 **7.4 GIA Gravity Fraction**
793 McKenzie [2010] also investigated a parameter β, which he defined as the fraction of the
794 joint convective-GIA gravity anomaly due to GIA, or
795 $$\beta = \frac{G_G}{G_{CG}} \tag{22}$$
796 Since $G_{CG} = G_C + G_G$, $G_C = Q_C H_C$, and $G_G = Q_G H_G$, we can derive an expression for β in
797 terms of η from equations (20) and (22) as
798 $$\beta = \left(1 + \frac{q_{CG}}{\eta}\right)^{-1} \tag{23}$$
799 where $q_{CG} = Q_C / Q_G$. Then, using equation (21), we can derive an equation linking β with the
800 parameter η' which we obtained during inversion; thus,

$$\beta = \left[1 + q_{CG} \left(\frac{1}{\eta'} - 1 \right) \right]^{-1} \quad (24)$$

We determine the errors on β from the estimated errors on η' by applying propagation of variances to equation (24), giving

$$\sigma_\beta = \frac{q_{CG}}{\left[(1 - q_{CG})\eta' + q_{CG} \right]^2} \sigma_{\eta'} \quad (25)$$

The errors on η' used in equation (25) were the mean of the upper and lower 95% confidence limits given in Table 3.

It is in the long-wavelength limit that H_C and H_G are most likely to be in phase (at least over the Canadian Shield). So to calculate a value for q_{CG}, we evaluated Q_C and Q_G using the theoretical equations (29) and (31), respectively, at a wavelength of 2000 km (which is approximately the longest wavelength resolved in regions A and B); used the best fitting T_e to compute Q_C; the densities and constants given in Table 1; and took their ratio.

Table 3 shows the β and σ_β values obtained by applying equations (24) and (25) to the best fitting η' and T_e values from the global admittance inversion. The value of β determined by Tamisiea et al. [2007] was 0.38 (or within a possible range of 0.25 to 0.45). Our values from both wavelets are slightly higher in region A, at around 0.5 to 0.6, but are more similar to the Tamisiea et al. [2007] value when the larger area (region B) is considered.

McKenzie [2010] does not directly quote a value of β obtained from his study but uses the long-wavelength observed admittance ($\bar{Q}_{O,0}$) value that he observed (64 ± 5 mGal/km) as a proxy. Therefore, Table 3 also shows the values of $\bar{Q}_{O,0}$ obtained from our studies. The 7.547-WT and 5.336-WT values are very similar to that of McKenzie [2010].

824

825 We choose not to display the spatial variations in η', as we do for T_e in Figures 8–11, because
826 the errors on this parameter are much larger than those on T_e and F (Table 3), and so the
827 spatial variations are likely to be statistically insignificant.

828

829 **8. Conclusions**

830 The free-air gravity/topography admittance over the Canadian Shield, calculated using
831 wavelet transforms, shows a characteristic dip at long wavelengths that is consistent with a
832 theoretical model incorporating mantle convection, GIA, and flexural response to loading.
833 Multitapers lack the resolution in wave number at long wavelengths that is required to show
834 this feature.

835

836 Inversion of the observed admittance suggests that the elastic thickness of the majority of the
837 Canadian Shield exceeds 80 km, with a higher-T_e core located near the southwest shore of
838 Hudson Bay. The periphery of the shield is characterized by lower elastic thicknesses, in
839 keeping with the findings of thermal studies. Furthermore, an analysis of the imaginary
840 component of the admittance has revealed that unexpressed loading ("noise") is not as
841 pervasive in the shield as our earlier study suggested [Kirby and Swain, 2009].

842

843 The high values of T_e over the Canadian Shield are consistent with estimates of the geotherm
844 based on (a) analyses of garnets from xenocrysts in kimberlites and (b) surface heat flow data
845 and shear velocity from seismic tomography, provided the crust and mantle are fully coupled,
846 anhydrous and subject to relatively small tectonic stresses.

847

Finally, the value we recover for the fraction of the long-wavelength gravity field due to glacial isostatic adjustment is in reasonable agreement with previous estimates for the region, at around 30–50%, though our estimates have large error bounds.

Appendix A: Models of Mantle Convection, GIA, and Flexure

A1. Mantle Convection

The synthetic gravity and topography due to mantle convection were generated using the equations provided in McKenzie [2010], with both determined from a temperature distribution, $t(\mathbf{x})$, at depth a below the Earth's surface. The Fourier transform of the gravity anomaly is obtained from equations (A9), (A13), and (A15)–(A17) of McKenzie [2010], giving

$$G_C = \frac{2\pi\mathcal{G}\alpha}{k}\left[\frac{3\rho_M}{4\Theta} - \frac{\rho_M ka}{2\sinh ka} + \frac{\Delta\rho_{Mf}\left(\cosh ka - 1\right)}{3\Theta\sinh ka}\right]T \tag{26}$$

where $k \equiv |\mathbf{k}|$ is radial wave number, $T(\mathbf{k})$ is the Fourier transform of $t(\mathbf{x})$, α is the thermal expansion coefficient, a is the lithosphere thickness, ρ_M is the density of the mantle, and ρ_f is the density of the overlying fluid (water or air – we use air with $\rho_f = 0$); we use the notation $\Delta\rho_{xy} = \rho_x - \rho_y$, and we define the parameter Θ as

$$\Theta = 1 + \frac{Dk^4}{\Delta\rho_{Mf}\, g} \tag{27}$$

where D is the flexural rigidity which is related to elastic thickness by $D = E T_e^3 / 12(1-\nu^2)$; see Table 1 (region A values) for symbols and values of constants. The Fourier transform of the topography due to mantle convection is obtained from equations (A9) and (A16) of McKenzie [2010], giving

$$H_C = \frac{\alpha}{k\Theta}\left[\frac{3\rho_M}{4\Delta\rho_{Mf}} + \frac{\cosh ka - 1}{3\sinh ka}\right]T \tag{28}$$

To obtain synthetic space domain grids of the gravity and topography due to mantle convection, the Fourier transforms in equations (26) and (28) are inverse transformed to the space domain.

875 Since $G_C = Q_C H_C$, an expression for the admittance due to mantle convection is derived from
876 the ratio of equations (26) and (28):

877 $$Q_C = 2\pi\mathcal{G}\Theta\left[\frac{3\rho_M}{4\Theta} - \frac{\rho_M ka}{2\sinh ka} + \frac{\Delta\rho_{Mf}\left(\cosh ka - 1\right)}{3\Theta\sinh ka}\right]\left[\frac{3\rho_M}{4\Delta\rho_{Mf}} + \frac{\cosh ka - 1}{3\sinh ka}\right]^{-1} \quad (29)$$

878 which is no longer dependent upon the constants α or T_0.

879

880 We will also find it useful to derive an expression for Q_C in its long-wavelength limit. As k
881 $\rightarrow 0$, equation (29) becomes

882 $$Q_{C,0} \simeq \tfrac{2}{3}\pi\mathcal{G}\Delta\rho_{Mf} \quad (30)$$

883 which takes a value of 47.5 mGal/km, for the mantle density we use (Table 1, region A).

884

885 **A2. GIA**

886 For a given topography due to GIA, $h_G(\mathbf{x})$, with Fourier transform $H_G(\mathbf{k})$, the transform of the
887 corresponding gravity field, G_G, is given by $G_G = Q_G H_G$, where Q_G is the GIA admittance.
888 For a three-layer crust, and based on equation (A26) of McKenzie [2010], this admittance is
889 given as

890 $$Q_G = 2\pi\mathcal{G}\left[\Delta\rho_{uf} + \Delta\rho_{mu}e^{-kz_u} + \Delta\rho_{lm}e^{-kz_m} + \Delta\rho_{Ml}e^{-kz_l}\right] \quad (31)$$

891 where ρ_u, ρ_m, and ρ_l are the densities of the upper, middle, and lower crust, respectively, and
892 z_u, z_m, and z_l are the depths to the bases of the upper, middle, and lower crust, respectively –
893 see Table 1 (region A values). Again, we use the notation $\Delta\rho_{xy} = \rho_x - \rho_y$. The long-
894 wavelength limit of equation (31) is obtained by setting $k = 0$, giving

895 $$Q_{G,0} \simeq 2\pi\mathcal{G}\Delta\rho_{Mf} \quad (32)$$

896 which takes a value of 142.5 mGal/km, for the mantle density we use (Table 1, region A).

897

898 **A3. Flexure**

899 Given two initial loads, surface and internal, $h_i(\mathbf{x})$ and $w_i(\mathbf{x})$, respectively, acting on a thin,
900 elastic plate of known T_e, the Fourier transforms of the free-air anomaly and topography after
901 flexure are given by

902 $$\begin{bmatrix} G_F \\ H_F \end{bmatrix} = \begin{bmatrix} \mu_B & \mu_T \\ \kappa_B & \kappa_T \end{bmatrix} \begin{bmatrix} W_i \\ H_i \end{bmatrix} \tag{33}$$

903 where capital letters denote Fourier transforms, and the matrix coefficients for a model with
904 three crustal layers and internal loading at the base of the upper crust are given by

905 $$\mu_B = \frac{2\pi\mathcal{G}}{\Phi g}\left[-\Delta\rho_{uf} + \left(\Phi - \Delta\rho_{mu}\right)e^{-kz_u} - \Delta\rho_{lm}e^{-kz_m} - \Delta\rho_{Ml}e^{-kz_l}\right] \tag{34}$$

906 $$\mu_T = \frac{2\pi\mathcal{G}}{\Phi g}\left[\left(\Phi - \Delta\rho_{uf}\right) - \Delta\rho_{mu}e^{-kz_u} - \Delta\rho_{lm}e^{-kz_m} - \Delta\rho_{Ml}e^{-kz_l}\right] \tag{35}$$

907 $$\kappa_B = \frac{-1}{\Phi g} \tag{36}$$

908 $$\kappa_T = \frac{1}{\Delta\rho_{uf} g} - \frac{1}{\Phi g} \tag{37}$$

909 where

910 $$\Phi = \frac{Dk^4}{g} + \Delta\rho_{Mf} \tag{38}$$

911 [e.g., Kirby and Swain, 2009, 2011]. See sections A1 and A2 and Table 1 for the definitions
912 and values of the symbols we use. Again, we use the notation $\Delta\rho_{xy} = \rho_x - \rho_y$.

913

914 An expression for the flexural admittance when the initial loads are uncorrelated can be
915 derived using the procedures outlined in Kirby and Swain [2009, 2011]:

916 $$Q_F = \frac{\mu_B\kappa_B f^2 + \mu_T\kappa_T}{\kappa_B^2 f^2 + \kappa_T^2} \tag{39}$$

In equation (39), f is the loading ratio between initial internal and surface loads, which is in principle wave number dependent, though has uniform values in this study. In this article we commonly express the loading ratio f in terms of the internal load fraction F, where

$$F = \frac{f}{1+f} \tag{40}$$

[McKenzie, 2003]. The long-wavelength limit of equation (39) is simply $Q_{F,0} = 0$.

A4. Combined Flexural, Convective, and GIA Admittance

Instead of combining only the admittances corresponding to convection and GIA as McKenzie [2010] did, we include the admittance due to flexural processes as follows. Dealing now with Fourier transforms of the fields, let the total observed free-air anomaly in the wave number domain be $G = G_C + G_G + G_F$, where G_C, G_G, and G_F are the contributions due to convection, GIA and flexure, respectively. Similarly, the total observed topography in the wave number domain is $H = H_C + H_G + H_F$. The combined admittance is then

$$Q_{CGF} = \frac{\langle GH^* \rangle}{\langle HH^* \rangle} = \frac{\left\langle Q_C |H_C|^2 + Q_C H_C H_G^* + Q_G H_G H_C^* + Q_G |H_G|^2 + Q_F |H_F|^2 \right\rangle}{\left\langle |H_C|^2 + H_C H_G^* + H_G H_C^* + |H_G|^2 + |H_F|^2 \right\rangle} \tag{41}$$

where we have (1) made the substitutions $G_C = Q_C H_C$, $G_G = Q_G H_G$, and $G_F = Q_F H_F$, where Q_C, Q_G, and Q_F are the admittances due to convection, GIA, and flexure, respectively, given earlier; and (2) assumed that the flexural topography is statistically uncorrelated with the topographies due to both convection and GIA, or $\langle H_C H_F^* \rangle = \langle H_G H_F^* \rangle = 0$, etc.

As discussed in section 4.1 we assume that the topographies from convection and GIA are in phase, related by a wave number independent parameter $\eta = H_G / H_C$, as in equation (20). Substitution of $H_G = \eta H_C$ into equation (41) yields, after some rearrangement, the combined admittance due to flexure, mantle convection, and GIA:

$$Q_{CGF} = \frac{\left\langle \left[\eta^2 Q_G + \eta \left(Q_G + Q_C \right) + Q_C \right] \left| H_C \right|^2 + Q_F \left| H_F \right|^2 \right\rangle}{\left\langle \left(\eta + 1 \right)^2 \left| H_C \right|^2 + \left| H_F \right|^2 \right\rangle} \tag{42}$$

The individual admittances, Q_C, Q_G, and Q_F are given by equations (29), (31), and (39), respectively. If η is zero (either by choice or from the results of inversion), then there is no GIA component to the admittance.

Note that in order to evaluate equation (42), whether for plotting or inversion of observed data, we must assume values or expressions for $\left| H_C \right|$ and $\left| H_F \right|$. Here we assume that both the flexural topography, $h_F(\mathbf{x})$, and temperature distribution at the top of the half-space, $t(\mathbf{x})$, have fractal spectra, with amplitude spectra in the wave number (k) domain of

$$H_F \left(k \right) = A_F \, k^{-\zeta_F} \tag{43}$$

for the flexural topography and

$$T \left(k \right) = A_T \, k^{-\zeta_T} \tag{44}$$

for the convective temperature, where ζ is the fractal exponent, related to the fractal dimension, FD, by FD = 4 – ζ. The amplitudes, A_F and A_T, are estimated from fan wavelet power spectra [Kirby and Swain, 2013] of the corresponding space domain data; more details can be found in the main text. During numerical evaluation of equation (42), the convective topography, H_C, is obtained by substituting the numerical values of $T(k)$ into equation (28).

Figure A1 shows several theoretical admittance curves for the combined convective, GIA, and flexural admittance, at different T_e values and at different values of A_F, in order to ascertain the sensitivity of the admittance to this parameter. We first note that the flexural-only admittance transition wavelength is not affected by the incorporation of the mantle convection and GIA signals. That is, the flexural regime is distinct from the effects of

963 convection and GIA, which manifest only in the long wavelengths, and is separated from
964 these by a dip in the admittance, no matter what the T_e value.
965
966 It does appear, though, that the long-wavelength admittance is sensitive to the assumed value
967 of A_F. Since we can only estimate A_F from the observed topography, which is a combination
968 of convective, GIA, and flexural topographic signals, we must accept some degree of error
969 when inverting the observed admittance, particularly for the value of η, less so for T_e (which
970 can be constrained by the flexural transition), and very little for F. For this reason, in Table
971 A1 we present results of inversions of the $|\mathbf{k}_0| = 7.547$ synthetic model admittances in Figure
972 5 (periodic data with $R_{CG} = 1$) for three fixed values of A_F (the original, and half and twice
973 that value) while keeping its fractal dimension and other parameters fixed. For the low-T_e
974 plate the recovered T_e values are all approximately within the 95% confidence limits of the
975 recovered T_e value using the known A_F. This is also almost true for the high-T_e plate.
976 Regarding the recovered F values, the same applies, but it does not for the recovered η'
977 values where uncertainty in A_F can lead to a considerable error.
978
979 We also did this for the North America region A data (halving and doubling the assumed A_F
980 value). Results are shown in Table A2. T_e varies from 143 to 182 km, η' varies from 0.25 to
981 0.5, while F changes relatively little.
982

Appendix B: The Effect of Noise on Coherence and Admittance

The issue of the effect of "noise" upon coherence and admittance estimates has been the subject of debate recently [McKenzie and Fairhead, 1997; McKenzie, 2003; Kirby and Swain, 2009]. McKenzie and Fairhead [1997] and McKenzie [2003] proposed that parts of the gravity field not predicted by flexural models would act as noise and could reduce the coherence between Bouguer anomaly and topography fields; this would then yield overestimates of T_e upon inversion since the Bouguer coherence transition ("rollover") would migrate to longer wavelengths. They also proposed a model whereby internal loads could feasibly generate a finite gravity anomaly without producing flexural topography, so-called "unexpressed loading" [Crosby, 2007]. Kirby and Swain [2009] confirmed these proposals but with the important condition that the noise spectrum had to have significant power at the wavelengths surrounding the observed Bouguer coherence rollover. They proposed that the noise could be identified by analysis of the normalized squared imaginary free-air coherency (SIC) rather than the free-air coherence as McKenzie and Fairhead [1997] and McKenzie [2003] had suggested. The reason for this was that the free-air coherence (or its real part: squared real coherency or SRC) is very sensitive to many influences that can still be explained by flexure, and a lowering of the free-air SRC did not necessarily imply the presence of noise [Kirby and Swain, 2009]. In contrast, the normalized free-air SIC is model independent and uniquely reveals the extent and influence of correlated/uncorrelated signals [Kirby and Swain, 2009].

McKenzie and Fairhead [1997] and McKenzie [2003] proposed the use of the free-air admittance, rather than Bouguer coherence, for T_e estimation. This is because the admittance should be much less sensitive to uncorrelated noise than the coherency [e.g., Wieczorek, 2007]. In this appendix we test this proposition using synthetic modeling. We first generated

1008 one set of topography and gravity (both Bouguer and free-air anomaly) fields from a pair of
1009 random fractal surfaces acting as initial loads on a plate of uniform T_e = 40 km, with an
1010 assigned load fraction of F = 0.5. Other parameters are given in the caption to Figure B1.
1011 Note that here we do not use average spectra over 100 models.
1012
1013 Next, we generated grids of noise in the gravity field due to unexpressed loading; the details
1014 of this type of noise and its creation are given in Kirby and Swain [2009] (where it is called
1015 "type-I" noise, i.e., unfiltered). The standard deviations of the noise grids were scaled to have
1016 several values, all multiples of the standard deviation of the free-air anomaly grid, ranging
1017 from ¼ to 8.
1018
1019 We then added the noise grids to the "raw" free-air and Bouguer anomalies, left the
1020 topography unaltered, and computed the global wavelet free-air admittance, free-air
1021 coherency, and Bouguer coherency using equations (4) and (13).
1022
1023 Results are shown in Figure B1. Also shown are the global power spectra (as computed using
1024 the fan wavelet transform) [Kirby and Swain, 2013] for the raw free-air and Bouguer
1025 anomalies and the respective noise field. As expected, the Bouguer SRC is sensitive to the
1026 noise amplitude and becomes affected when the noise power is greater than or equal to the
1027 Bouguer anomaly power at the rollover wavelength. The normalized free-air SIC becomes
1028 nonzero when the noise power is greater than or equal to the free-air anomaly power at the
1029 rollover wavelength, as described in Kirby and Swain [2009]. The free-air SRC is more
1030 affected by noise than the Bouguer SRC.
1031

However, the free-air admittance is much less sensitive to added noise than is the free-air SRC. At noise power levels that cause the free-air SRC to deviate from theoretical predictions, the free-air admittance is largely unaltered. Indeed, the real free-air admittance only becomes seriously affected at comparatively high noise levels. In Figure B1 the imaginary component reaches large values, yet the real component still follows the general trend of the model prediction.

We conclude that if the free-air SRC (coherence) is used as an indicator of noise, then the effect of noise may be grossly overestimated (notwithstanding the points mentioned at the start of this appendix), certainly with regard to its effect upon the free-air admittance. We can also conclude that the free-air admittance is usually robust enough to provide useful T_e estimates, subject to an analysis of its imaginary part.

Acknowledgements

This work was supported by ARC grant DP0878453 and computations carried out on the Pawsey Centre's Epic supercomputer. The figures were plotted using GMT [Wessel and Smith, 1998]. This is TIGeR publication 512.

1050 **References**

1051 Antoine, J.-P., R. Murenzi, P. Vandergheynst, and S. T. Ali (2004), *Two-Dimensional*
1052 *Wavelets and Their Relatives*, Cambridge University Press, Cambridge, 458 pp.

1053 Audet, P., and J.-C. Mareschal (2004a), Variations in elastic thickness in the Canadian
1054 Shield, *Earth Planet. Sci. Lett.*, *226*, 17-31.

1055 Audet, P., and J.-C. Mareschal (2004b), Anisotropy of the flexural response of the lithosphere
1056 in the Canadian Shield, *Geophys. Res. Lett.*, *31*, L20601, doi:10.1029/2004GL021080.

1057 Audet, P., and J.-C. Mareschal (2007), Wavelet analysis of the coherence between Bouguer
1058 gravity and topography: Application to the elastic thickness anisotropy in the Canadian
1059 Shield, *Geophys. J. Int.*, *168*, 287-298.

1060 Bassin, C., G. Laske, and G. Masters (2000), The current limits of resolution for surface wave
1061 tomography in North America, *EOS Trans. Am. Geophys. Union*, *81*, F897.

1062 Bechtel, T. D., D. W. Forsyth, V. L. Sharpton, and R. A. F. Grieve (1990), Variations in
1063 effective elastic thickness of the North American lithosphere, *Nature, 343***,** 636-638.

1064 Bendat, J. S., and A. G. Piersol (2000), *Random Data: Analysis and Measurement*
1065 *Procedures*, 3rd ed., John Wiley, New York, 594 pp.

1066 Bracewell, R. N. (1986), *The Fourier Transform and Its Applications*, McGraw-Hill, New
1067 York, 474 pp.

1068 Brodholt, J. (2013), Water may be a damp squib, *Nature, 498*, 181-182.

1069 Burov, E. B., and M. Diament (1995), The effective elastic thickness (T_e) of continental
1070 lithosphere: What does it really mean? *J. Geophys. Res.*, *100*(B3), 3905-3927.

1071 Burov, E., and M. Diament (1996), Isostasy, equivalent elastic thickness, and inelastic
1072 rheology of continents and oceans, *Geology, 24*, 419-422.

1073 Chen, W.-P., and Z. Yang (2004), Earthquakes beneath the Himalayas and Tibet: Evidence
1074 for a strong lithospheric mantle, *Science, 304*, 1949-1952.

1075 Crosby, A. G. (2007), An assessment of the accuracy of admittance and coherence estimates
1076 using synthetic data, *Geophys. J. Int.*, *171*, 25-54.
1077 Fei, H., M. Wiedenbeck, D. Yamazaki, and T. Katsura (2013), Small effect of water on
1078 upper-mantle rheology based on silicon self-diffusion coefficients, *Nature*, *498*, 213-216.
1079 Forsyth, D. W. (1985), Subsurface loading and estimates of the flexural rigidity of
1080 continental lithosphere, *J. Geophys. Res.*, *90*(B14), 12,623-12,632.
1081 Griffin, W. L., S. Y. O'Reilly, B. J. Doyle, N. J. Pearson, H. Coopersmith, K. Kivi, V.
1082 Malkovets, and N. Pokhilenko (2004), Lithosphere mapping beneath the North American
1083 plate, *Lithos*, *77*, 873-922.
1084 Jackson, J. (2002), Strength of the continental lithosphere: Time to abandon the jelly
1085 sandwich? *GSA Today*, *12*, 4-10.
1086 Kirby, J. F. (2005), Which wavelet best reproduces the Fourier power spectrum? *Comput.*
1087 *Geosci.*, *31*, 846-864.
1088 Kirby, J. F., and C. J. Swain (2004), Global and local isostatic coherence from the wavelet
1089 transform, *Geophys. Res. Lett.*, *31*, L24608, doi:10.1029/2004GL021569.
1090 Kirby, J. F., and C. J. Swain (2009), A reassessment of spectral T_e estimation in continental
1091 interiors: The case of North America, *J. Geophys. Res.*, *114*, B08401,
1092 doi:10.1029/2009JB006356.
1093 Kirby, J. F., and C. J. Swain (2011), Improving the spatial resolution of effective elastic
1094 thickness estimation with the fan wavelet transform, *Comput. Geosci.*, *37*, 1345-1354.
1095 Kirby, J. F., and C. J. Swain (2013), Power spectral estimates using two-dimensional Morlet-
1096 fan wavelets with emphasis on the long wavelengths: Jackknife errors, bandwidth
1097 resolution and orthogonality properties, *Geophys. J. Int.*, *194*, 78-99.

1098 Kopylova, M. G., J. K. Russell, and H. Cookenboo (1999), Petrology of peridotite and
1099 pyroxenite xenoliths from the Jericho kimberlite: Implications for the thermal state of the
1100 mantle beneath the Slave craton, northern Canada, *J. Petrol.*, *40*, 79-104.
1101 Lee, T. S. (1996), Image representation using 2D Gabor wavelets, *IEEE Trans. Pattern Anal.*
1102 *Mach. Intell.*, *18*, 959-971.
1103 Lévy, F., C. Jaupart, J.-C. Mareschal, G. Bienfait, and A. Limare (2010), Low heat flux and
1104 large variations of lithospheric thickness in the Canadian Shield, *J. Geophys. Res.*, *115*,
1105 B06404, doi:10.1029/2009JB006470.
1106 Li, Z.-X. A., C.-T. A. Lee, A. H. Peslier, A. Lenardic, and S. J. Mackwell (2008), Water
1107 contents in mantle xenoliths from the Colorado Plateau and vicinity: Implications for the
1108 mantle rheology and hydration-induced thinning of continental lithosphere, *J. Geophys.*
1109 *Res.*, *113*, B09210, doi:10.1029/2007JB005540.
1110 Lowry, A. R., and R. B. Smith (1995), Strength and rheology of the western U.S. Cordillera,
1111 *J. Geophys. Res.*, *100*(B9), 17,947-17,963.
1112 Macario, A., A. Malinverno, and W. F. Haxby (1995), On the robustness of elastic thickness
1113 estimates obtained using the coherence method, *J. Geophys. Res.*, *100*(B8), 15,163-15,172.
1114 Maggi, A., J. A. Jackson, D. McKenzie, and K. Priestley (2000), Earthquake focal depths,
1115 effective elastic thickness, and the strength of the continental lithosphere, *Geology*, *28*, 495-
1116 498.
1117 McKenzie, D. (2003), Estimating T_e in the presence of internal loads, *J. Geophys. Res.*,
1118 *108*(B9), 2438, doi:10.1029/2002JB001766.
1119 McKenzie, D. (2010), The influence of dynamically supported topography on estimates of T_e,
1120 *Earth Planet. Sci. Lett.*, *295*, 127-138.

McKenzie, D., and J. D. Fairhead (1997), Estimates of the effective elastic thickness of the continental lithosphere from Bouguer and free air gravity anomalies, *J. Geophys. Res.*, *102*(B12), 27,523-27,552.

Munk, W. H., and D. E. Cartwright (1966), Tidal spectroscopy and prediction, *Philos. Trans. R. Soc. London, Ser. A, 259*, 533-581.

Pavlis, N. K., S. A. Holmes, S. C. Kenyon, and J. K. Factor (2012), The development and evaluation of the Earth Gravitational Model 2008 (EGM2008), *J. Geophys. Res.*, *117*, B04406, doi:10.1029/2011JB008916 (Correction, *J. Geophys. Res.*, doi:10.1002/jgrb.50167, 2013).

Pawlak, A., D. W. Eaton, I. D. Bastow, J.-M. Kendall, G. Helffrich, J. Wookey, and D. Snyder (2011), Crustal structure beneath Hudson Bay from ambient-noise tomography: implications for basin formation, *Geophys. J. Int. 184*, 65-82.

Pérez-Gussinyé, M., A. R. Lowry, A. B. Watts, and I. Velicogna (2004), On the recovery of effective elastic thickness using spectral methods: Examples from synthetic data and from the Fennoscandian Shield, *J. Geophys. Res.*, *109*(B10), B10409, doi:10.1029/2003JB002788.

Peslier, A.H., A. B. Woodland, D. R. Bell, and M. Lazarov (2010), Olivine water contents in the continental lithosphere and the longevity of cratons, *Nature, 467*, 78-81.

Pilkington, M. (1991), Mapping elastic lithospheric thickness variations in Canada, *Tectonophysics*, *190*, 283-297.

Pollack, H. N. (1986), Cratonization and thermal evolution of the mantle, *Earth Planet. Sci. Lett.*, *80*, 175-182.

Press, W. H., S. A. Teukolsky, W. T. Vetterling, and B. P. Flannery (1992), *Numerical Recipes in Fortran 77*, 2nd ed., Cambridge University Press, Cambridge.

1145 Saupe, D. (1988), Algorithms for random fractals, in *The Science of Fractal Images*, edited
1146 by H.-O. Peitgen and D. Saupe, pp. 71-136, Springer, New York.
1147 Simons, F. J., M. T. Zuber, and J. Korenaga (2000), Isostatic response of the Australian
1148 lithosphere: Estimation of effective elastic thickness and anisotropy using multitaper
1149 spectral analysis, *J. Geophys. Res.*, *105*(B8), 19,163-19,184.
1150 Simons, F. J., R. D. van der Hilst, and M. T. Zuber (2003), Spatiospectral localization of
1151 isostatic coherence anisotropy in Australia and its relation to seismic anisotropy:
1152 Implications for lithospheric deformation, *J. Geophys. Res.*, *108*(B5), 2250,
1153 doi:10.1029/2001JB000704.
1154 Slepian, D. (1978), Prolate spheroidal wave functions, Fourier analysis, and uncertainty – V:
1155 The discrete case, *Bell Syst. Tech. J.*, *57*, 1371-1430.
1156 Sloan, R. A., and J. A. Jackson (2012), Upper-mantle earthquakes beneath the Arafura Sea
1157 and south Aru Trough: Implications for continental rheology, *J. Geophys. Res.*, *117*,
1158 B05402, doi:10.1029/2011JB008992.
1159 Smith, W. H. F., and P. Wessel (1990), Gridding with continuous curvature splines in
1160 tension, *Geophysics*, *55*, 293-305.
1161 Stephenson, R., and C. Beaumont (1980), Small-scale convection in the upper mantle and the
1162 isostatic response of the Canadian shield, in *Mechanisms of Continental Drift and Plate*
1163 *Tectonics*, edited by P. A. Davies and S. K. Runcorn, pp. 111-122, Academic Press, San
1164 Diego.
1165 Tamisiea, M. E., J. X. Mitrovica, and J. L. Davis (2007), GRACE gravity data constrain
1166 ancient ice geometries and continental dynamics over Laurentia, *Science*, *316*, 881-883.
1167 Tarantola, A. (1987), *Inverse Problem Theory*, Elsevier, Amsterdam.
1168 Thomson, D. J. (1982), Spectrum estimation and harmonic-analysis, *Proc. IEEE*, *70*, 1055-
1169 1096.

1170 Thomson, D. J. (2007), Jackknifing multitaper spectrum estimates, *IEEE Signal Process.*
1171 *Mag.*, *24*, 20-30.
1172 Thomson, D. J., and A. D. Chave (1991), Jackknifed error estimates for spectra, coherences,
1173 and transfer functions, in *Advances in Spectrum Analysis and Array Processing*, vol. 1,
1174 edited by S. Haykin, pp. 58-113, Prentice Hall, Englewood Cliffs, N.J.
1175 Torrence, C., and G. P. Compo (1998), A practical guide to wavelet analysis, *Bull. Am.*
1176 *Meteorol. Soc.*, *79*, 61-78.
1177 Wang, Y., and J.-C. Mareschal (1999), Elastic thickness of the lithosphere in the Central
1178 Canadian Shield, *Geophys. Res. Lett.*, *26***,** 3033-3035.
1179 Watts, A. B. (2001), *Isostasy and Flexure of the Lithosphere*, Cambridge University Press,
1180 Cambridge, 458 pp.
1181 Wessel, P., and W. H. F. Smith (1998), New, improved version of Generic Mapping Tools
1182 released, *EOS Trans. Am. Geophys. Union*, *79*, 579.
1183 Wieczorek, M. A. (2007), Gravity and topography of the terrestrial planets, in *Treatise on*
1184 *Geophysics*, vol. 10, edited by G. Schubert, pp. 165-206, Elsevier, Amsterdam.
1185

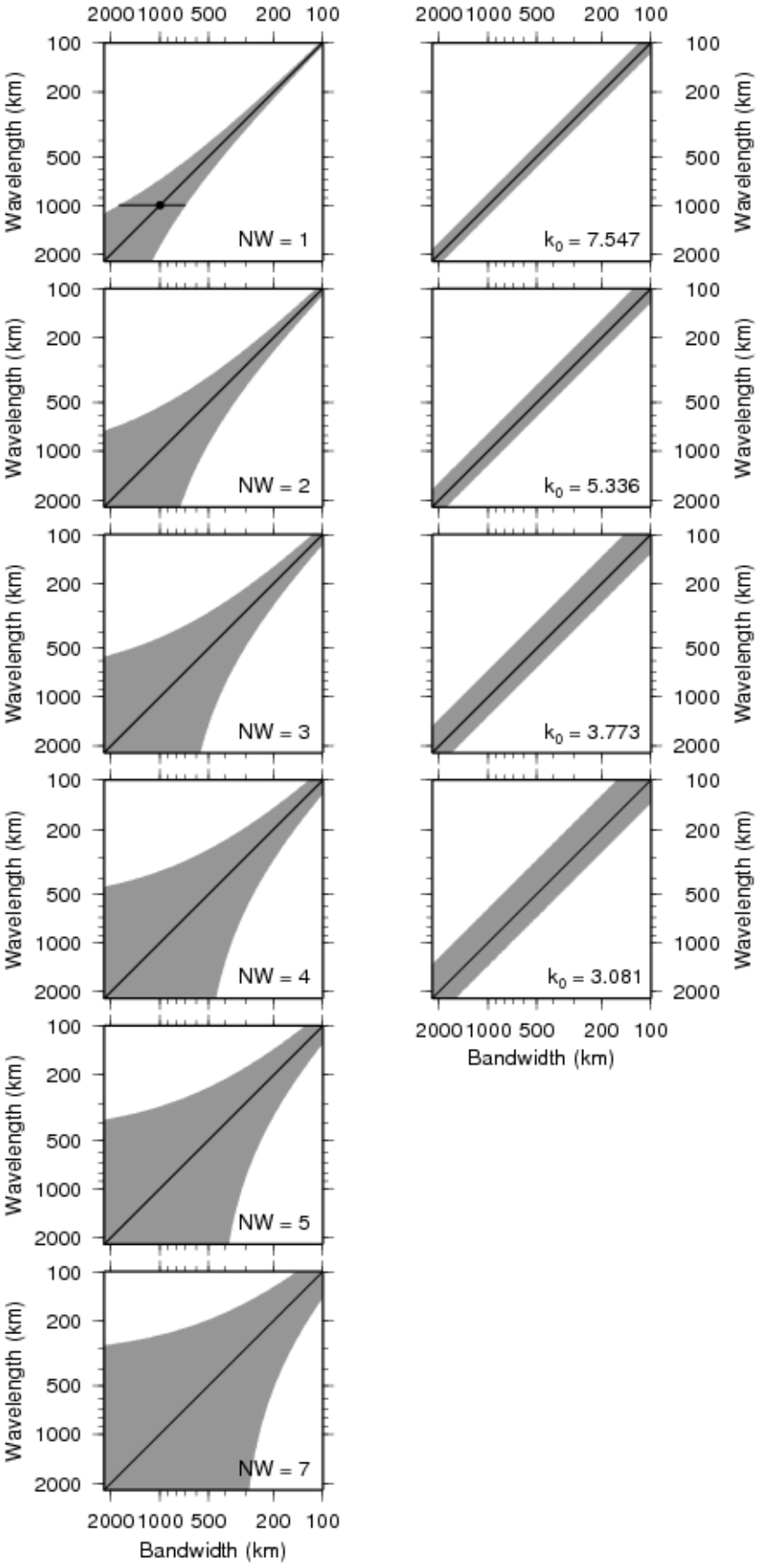
2000 1000 500 200 100
Wavelength (km)
100
200
500
1000
2000
NW = 1
NW = 2
NW = 3
NW = 4
NW = 5
NW = 7
k_0 = 7.547
k_0 = 5.336
k_0 = 3.773
k_0 = 3.081
Bandwidth (km)

1186

1187 Figure 1. Bandwidth resolution for the multitaper method (left column) at several values of
1188 NW (calculated using L = 2280 km in equation (16)) and for the Morlet-fan wavelet method
1189 (right column) at several values of $|\mathbf{k}_0|$. The black line is locus of $\lambda = \lambda$, for a wavelength λ,
1190 while the gray shading shows the half bandwidth of the two methods either side of the actual
1191 wavelength. For example, the NW = 1 panel shows the bandwidth at a wavelength of λ =
1192 1000 km, extending to 1781 km on the longer wavelength side and to 695 km on the shorter
1193 wavelength side.
1194

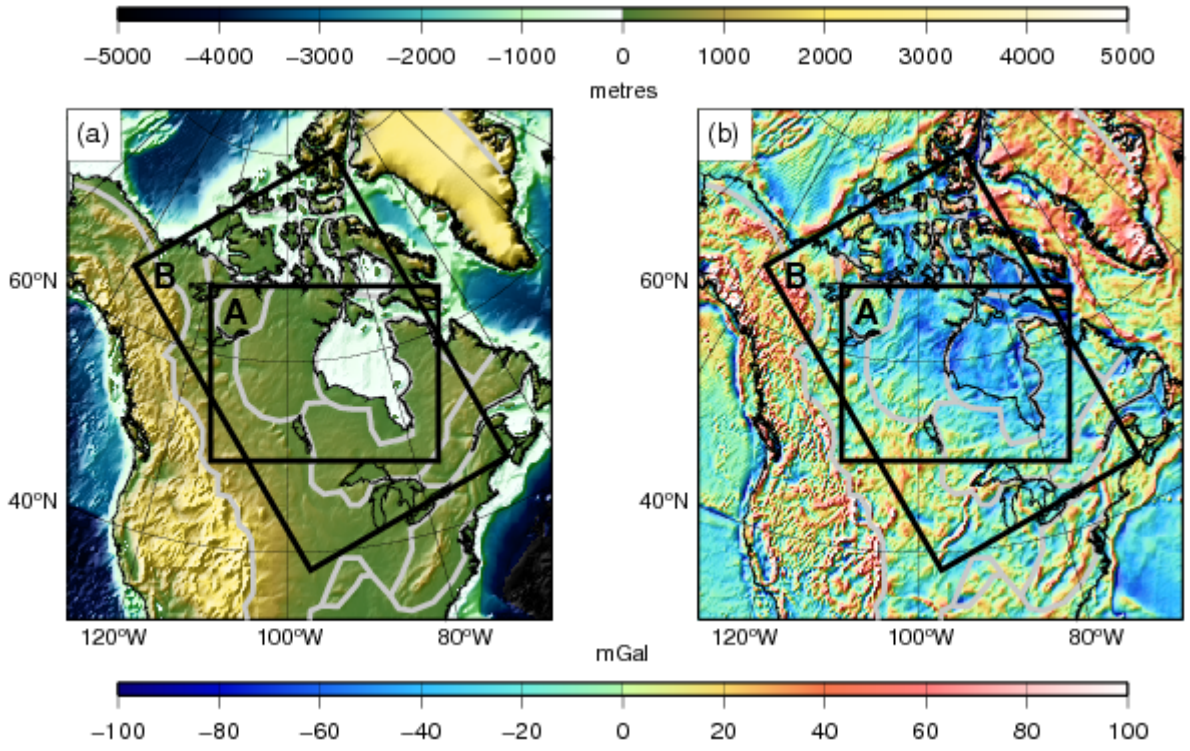

Figure 2. (a) Topography and (b) free-air anomaly of North America, showing the two study areas: region A and region B; Lambert conic conformal projections. Also marked in gray are the major geological province boundaries.

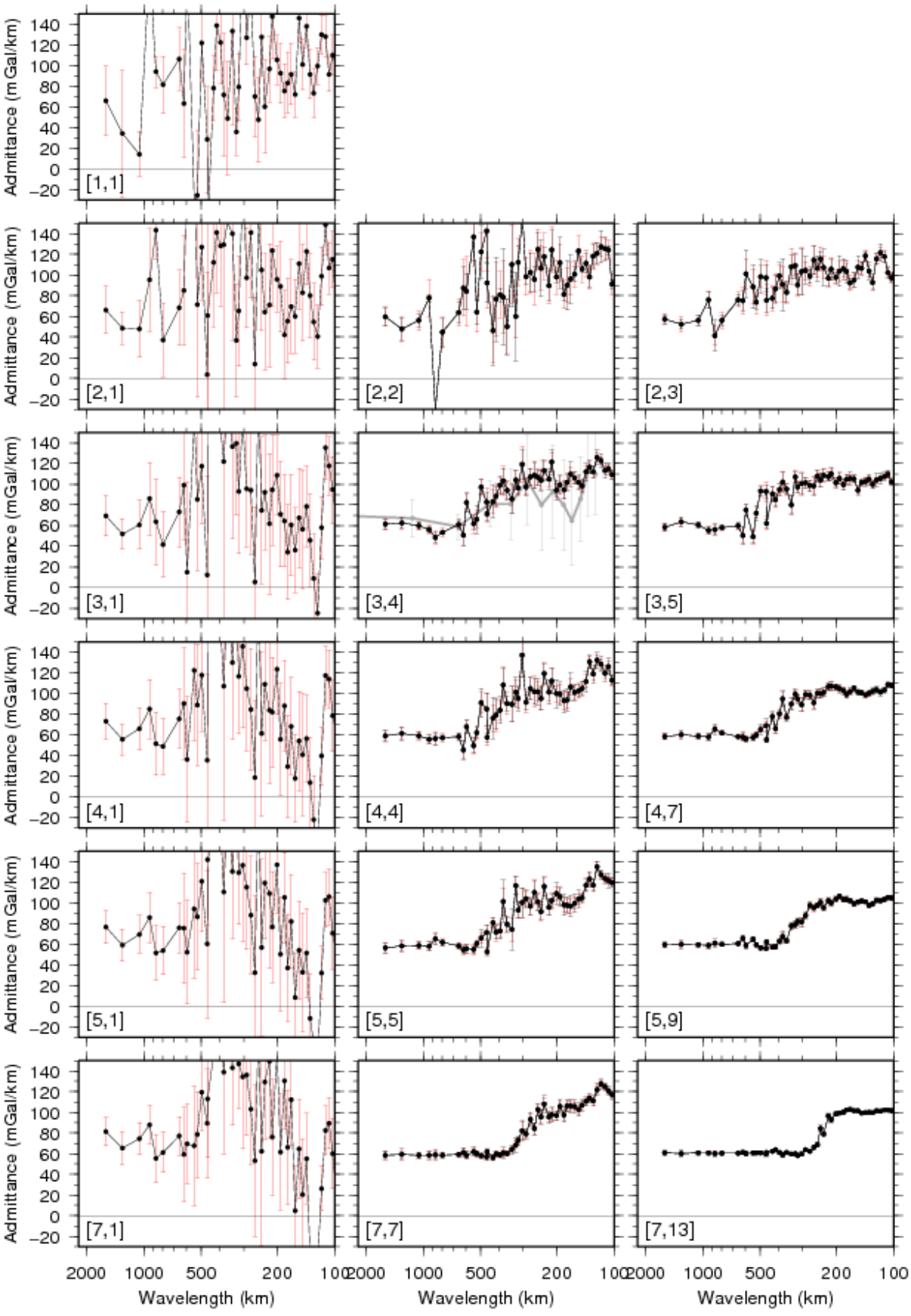
Admittance (mGal/km)
140
120
100
80
60
40
20
0
−20
[1,1]
[2,1]
[2,2]
[2,3]
[3,1]
[3,4]
[3,5]
[4,1]
[4,4]
[4,7]
[5,1]
[5,5]
[5,9]
[7,1]
[7,7]
[7,13]
2000
1000
500
200
100
Wavelength (km)

1200

1201 Figure 3. Multitaper admittances for region A using tapers of parameters [NW, *K*] as
1202 indicated in the panels. Error bars computed using the analytic equation (8) (red) and the
1203 jackknife method (black). The [3, 4] panel also shows the admittance data from Figure 4f of
1204 McKenzie [2010], in gray.
1205

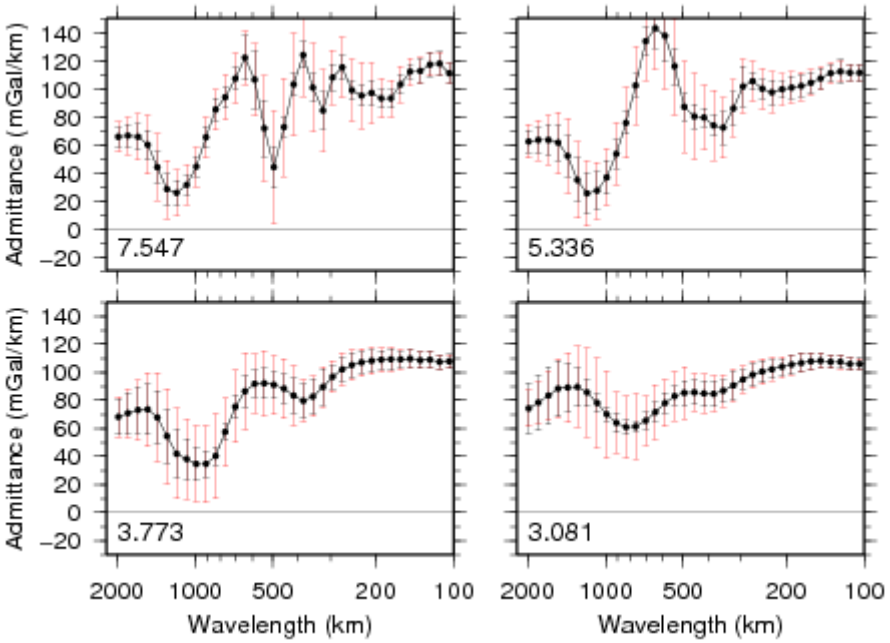

Figure 4. Global wavelet admittance for region A using Morlet-fan wavelets of $|\mathbf{k}_0|$ as indicated in the panels, with an e^{-1} cone of influence applied. Error bars computed using the analytic equation (8) (red), and the jackknife method (black).

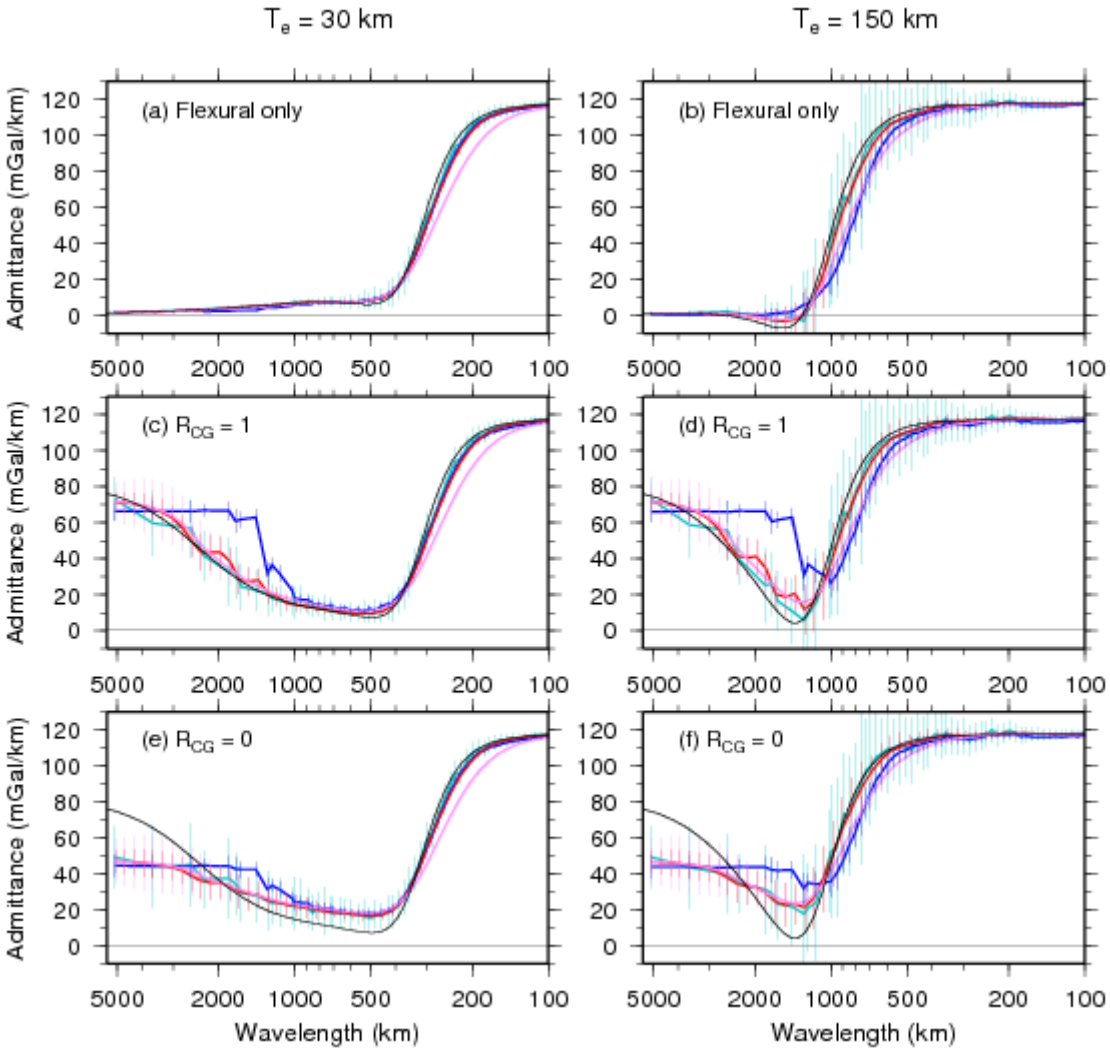

Figure 5. Admittances from synthetic models of (a and b) flexure, and (c, d, e and f) combined mantle convection, GIA, and flexure, using periodic space domain data. Admittance curves and errors are averages over the 100 models. Figures 5a, 5c, and 5e show admittances from synthetic plates with T_e = 30 km; Figures 5b, 5d, and 5f show admittances from synthetic plates with T_e = 150 km. The curves show results from the wavelet method with $|\mathbf{k}_0|$ = 7.547 (red) and 3.773 (pink) and from the multitaper method with [NW, K] of [1, 1] (cyan) and [3, 4] (blue). Error bars are from the jackknife method. The black lines show the theoretical admittance predictions for the models from equation (42). The parameter R_{CG} is the correlation coefficient between the space domain grids of convective and GIA topography, as explained in section 4.1. Note that the theoretical admittances in Figures 5e

and 5f are duplicates of those in Figures 5c and 5d because we have not developed an admittance model when $R_{CG} = 0$.

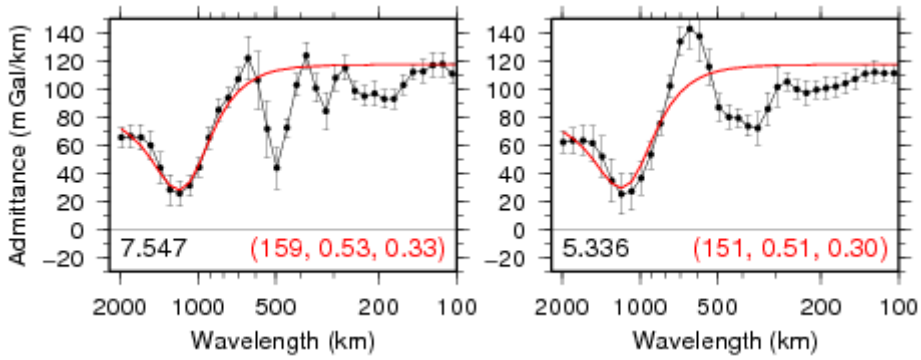

Figure 6. Admittances for North America, region A, computed using the fan wavelet method with the indicated $|\mathbf{k}_0|$ values. Observed free-air admittances and their jackknife error bars are the black circles and lines (as in Figures 3 and 4), and the best fitting predicted free-air admittances from a combined convection/GIA/flexural model are the red lines. The numbers in red are the best fitting (T_e, F, and η') values – see Table 3 for error bounds. Both admittance profiles were inverted over the whole spectrum.

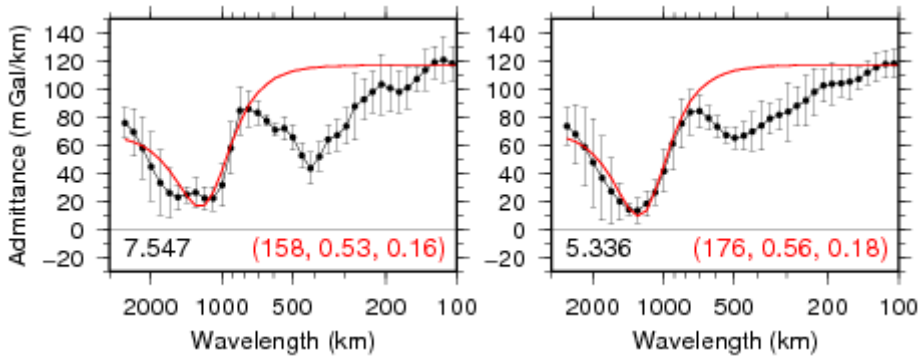

1233

1234 Figure 7. As in Figure 6 but for North American region B. Both admittance profiles were

1235 inverted only using observations with wavelengths >800 km.

1236

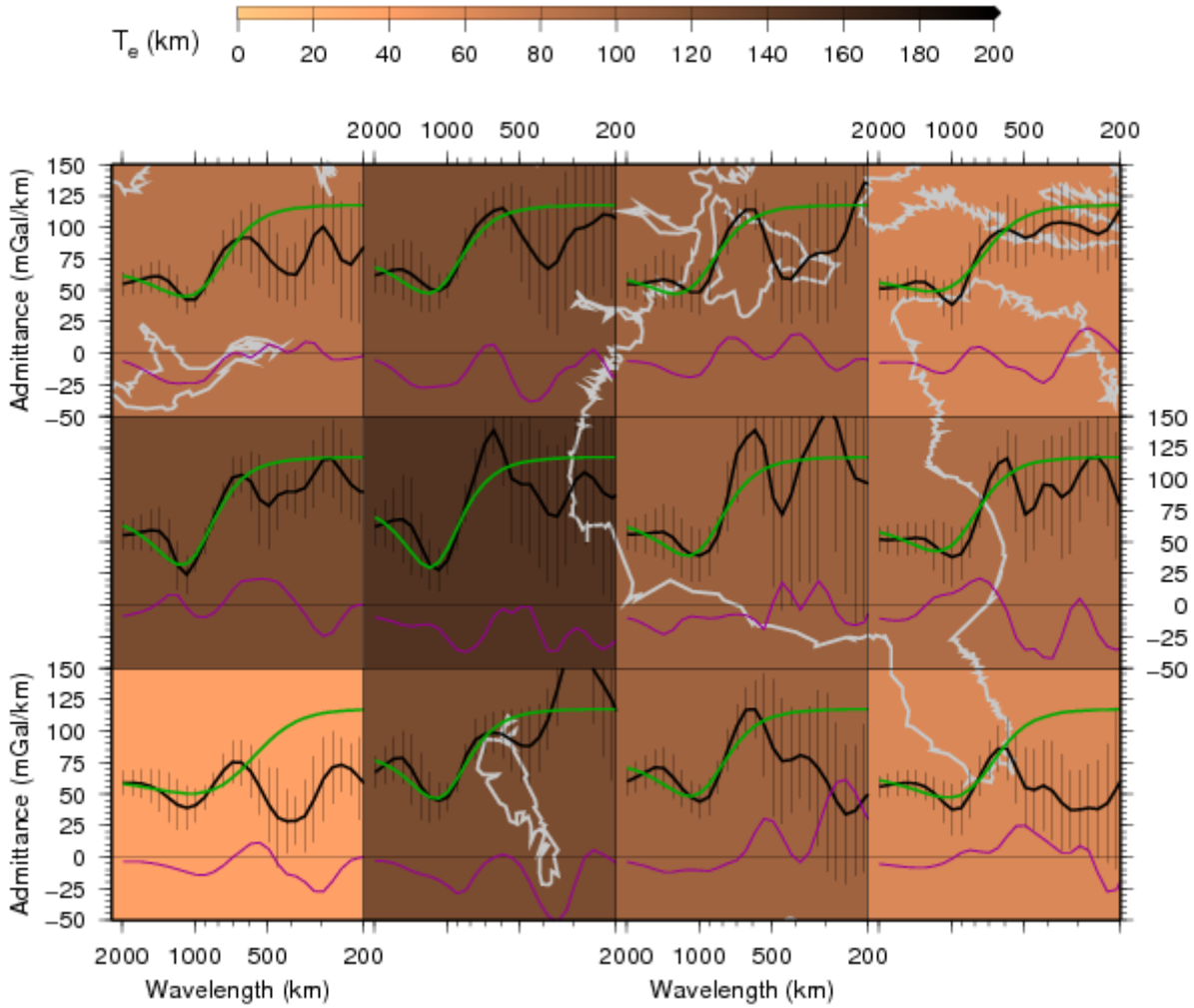

Figure 8. The spatial distribution of best fitting T_e and observed real (black) and imaginary (purple) admittances and best fitting predicted admittances (green) for North American region A, using wavelets of $|\mathbf{k}_0| = 5.336$. The autospectra and cross-spectra were averaged over spatial dimensions of 640×640 km and the observed admittance formed from these. Inversions were performed only on observed admittances with wavelengths >500 km. The coastline is shown in gray.

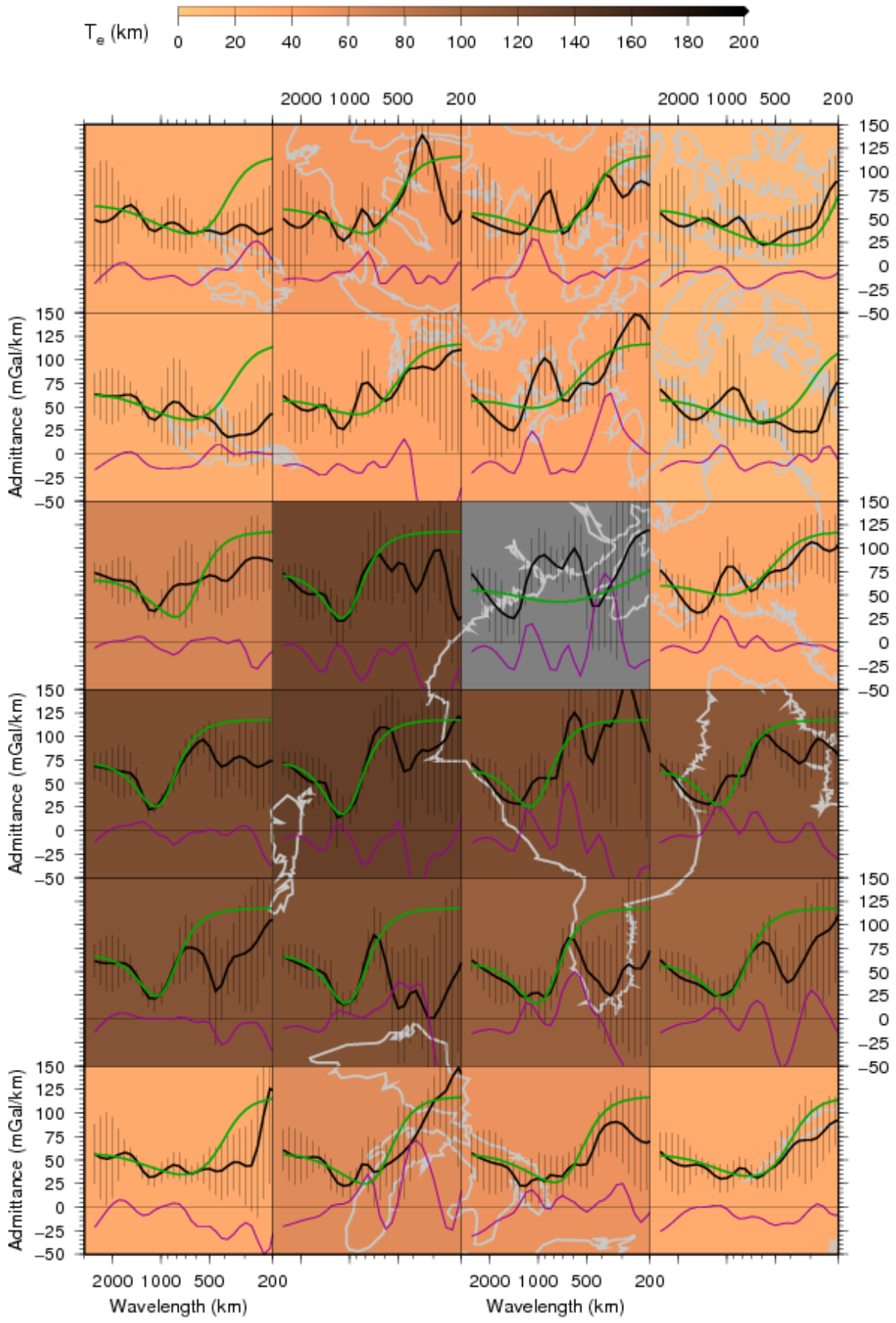
T_e (km)
0 20 40 60 80 100 120 140 160 180 200
2000 1000 500 200
Admittance (mGal/km)
150 125 100 75 50 25 0 −25 −50
Wavelength (km)

1245

1246 Figure 9. As in Figure 8 but for North American region B. The gray cell denotes that no
1247 suitable fit to the observed admittance could be found.
1248

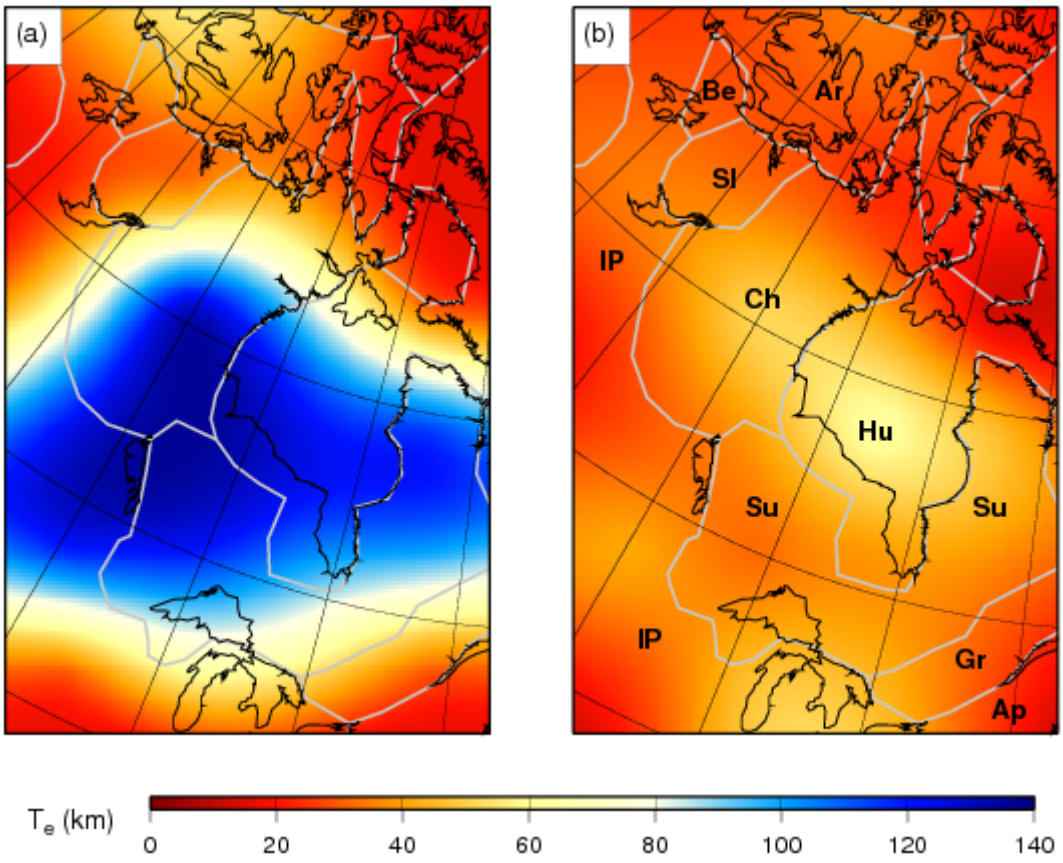

Figure 10. Smoothed and interpolated maps of (a) T_e and (b) its error over region B ($|\mathbf{k}_0|$ = 5.336). The 640×640 km T_e grid from Figure 9 formed the data that were interpolated to a 20×20 km grid using a minimum curvature algorithm [Smith and Wessel, 1990]. The major provinces are bounded with the gray lines: IP, Interior Platform; Su, Superior; Ch, Churchill; Sl, Slave; Be, Bear; Gr, Grenville; Ar, Arctic platform; Hu, Hudson Platform; Ap, Appalachian orogen. The Canadian Shield, with its exposed Precambrian rocks, comprises the Bear, Slave, Churchill, Superior and Grenville provinces. While not technically part of the shield, the Hudson and Interior Platforms consist of Precambrian basement overlain by Phanerozoic sedimentary rocks.

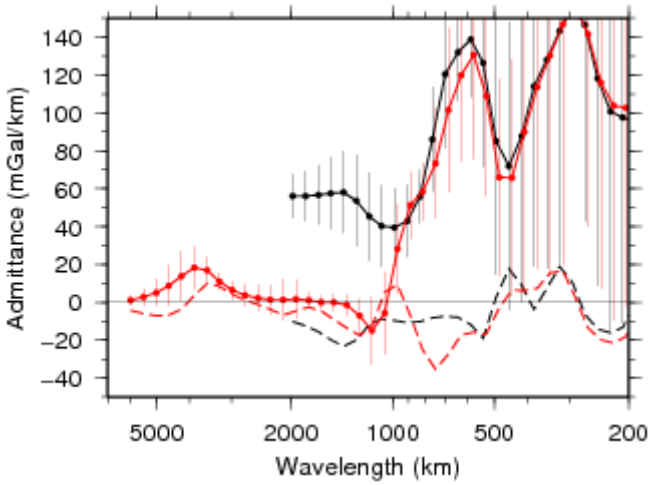

Figure 11. Observed admittance over Hudson Bay (real part solid with error bars; imaginary part dashed). The black curves are taken from cell 3 along and 2 up in Figure 8. The red curves were computed from gravity and topography data covering the entire continent, with the ($|\mathbf{k}_0|$ = 5.336) autospectra and cross-spectra spatially averaged over the same 640×640 km area that generated the black curves.

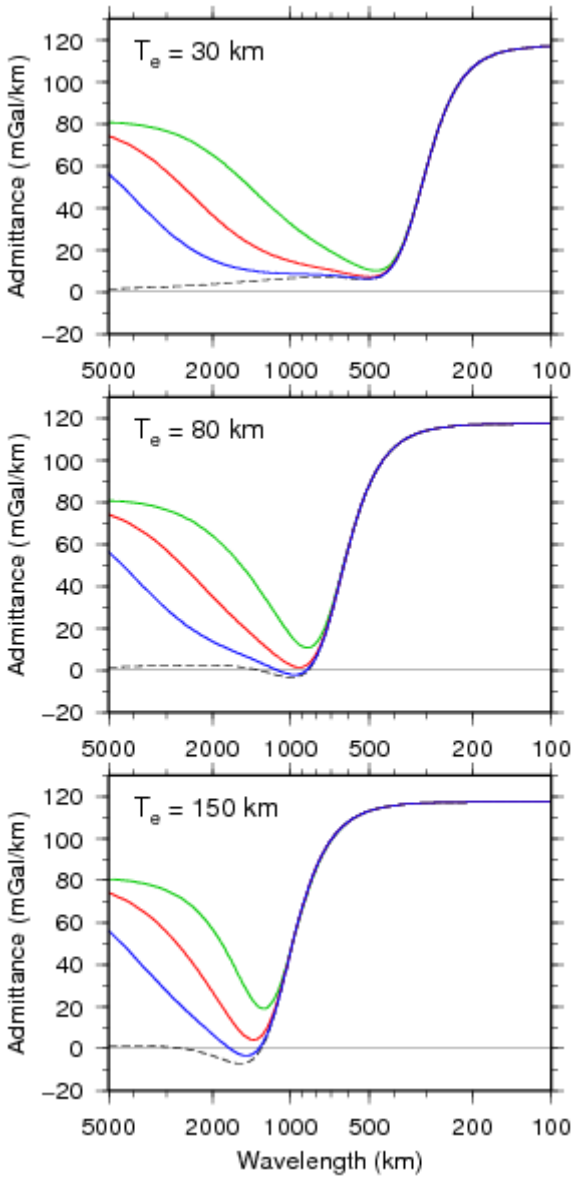

Figure A1. Theoretical admittance curves describing the combined mantle convection, GIA, and flexural admittance from equation (42), for three T_e values and three values of A_F, the spectral amplitude of the flexural topography in equation (43): 1.6×10^{-6} (green), 3.2×10^{-6} (red), and 6.4×10^{-6} (blue). Also plotted is the flexural-only admittance for the model T_e (dashed black). Other parameters used to generate the curves are the following: $F = 0.5$, $\eta = 0.5$, $a = 220$ km, $\zeta_F = 1.5$, $T(k) = 2.7\times10^{-10}\ k^{-2}$, with other parameters given in Table 1.

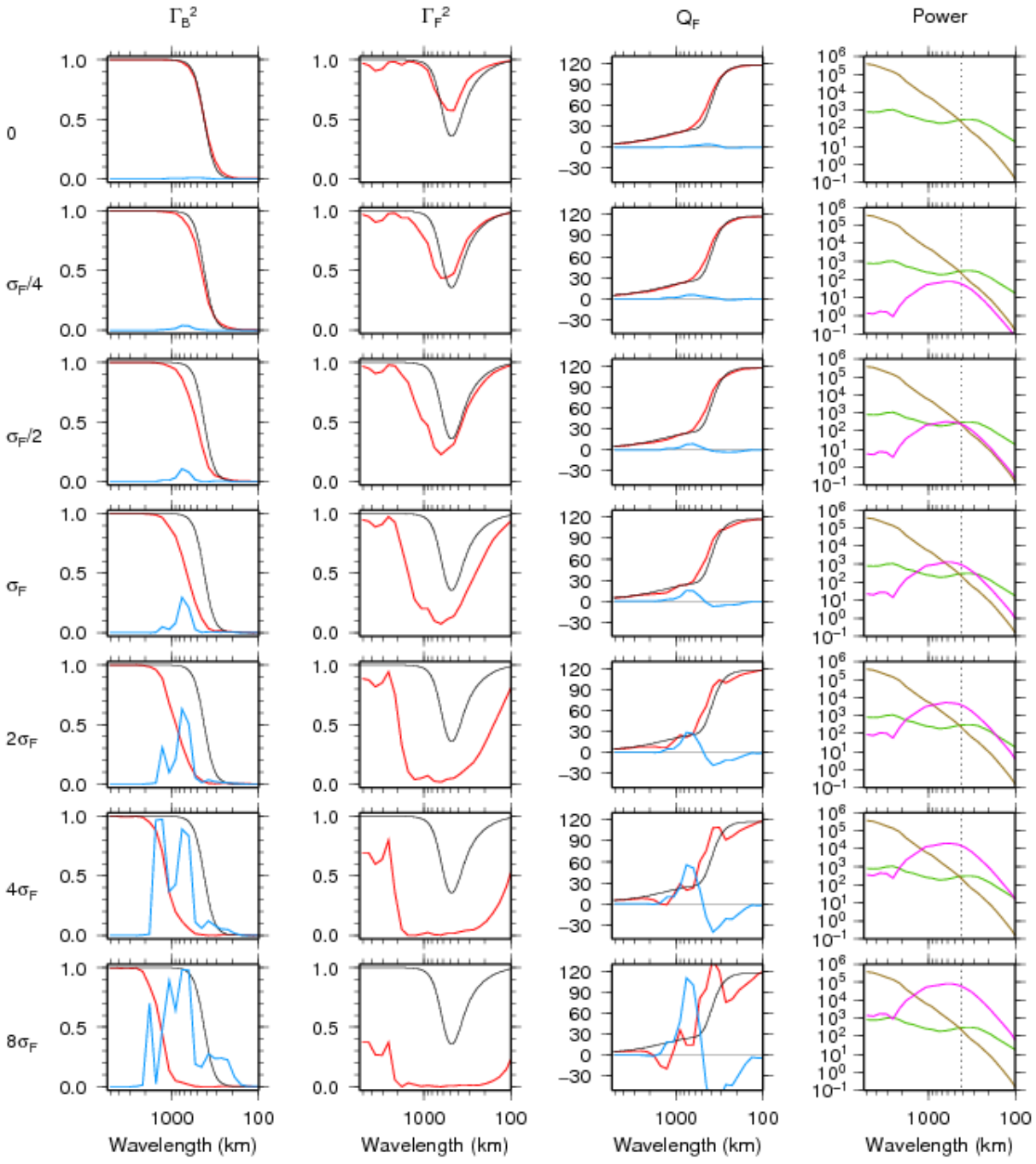

Figure B1. Showing the effect of noise upon the Bouguer coherence (SRC, Γ_B^2, first column), free-air coherence (SRC, Γ_F^2, second column), and (real) free-air admittance (Q_F, third column, units in mGal/km). The noise in this figure is "unexpressed loading noise" and was added to the gravity anomaly. The black curves show the theoretical, flexure-only predictions for the quantity for T_e = 40 km and F = 0.5; the red curves show the observed quantity recovered from wavelet analysis of the model; the blue curves show the normalized squared

imaginary free-air coherency (first column), and the imaginary free-air admittance (third column) from the wavelet analysis. The fourth column shows the global fan wavelet power spectrum of the raw free-air anomaly (green), the raw Bouguer anomaly (brown), and that of the noise field (pink). The vertical dotted line in the fourth column shows the wavelength of the theoretical Bouguer SRC rollover (422 km), which is also almost equal to the wavelength of the transition from low to high free-air admittance. The rows in the figure correspond to various noise amplitudes, given as a multiple of the standard deviation of the free-air anomaly (indicated at left). The top row corresponds to no added noise.

1291 **Tables**

	Region A		Region B	
	Density ($kg\ m^{-3}$)	**Depth to base (km)**	**Density ($kg\ m^{-3}$)**	**Depth to base (km)**
Upper crust	2800	13.8	2795	14.3
Middle crust	2860	27.1	2865	27.7
Lower crust	2980	39.2	2996	39.5
Mantle	3400	N/A	3396	N/A

1292

1293 Table 1. Mean densities and depths to base of indicated layers in North American regions A
1294 and B, from the CRUST2.0 model [Bassin et al., 2000]. In the flexural component of the
1295 combined convection-GIA-flexural inversions, internal loading was assumed to lie at the base
1296 of the upper crust. The densities and depths for region A were also used to generate the
1297 synthetic models and to invert the observed admittances. Other constants used in the
1298 inversions are the following: Young's modulus, E = 100 GPa; Poisson's ratio, ν = 0.25;
1299 gravity acceleration, g = 9.79 ms^{-2}; Newtonian gravitational constant, $\mathcal{G} = 6.67259\times10^{-11}$
1300 $m^3kg^{-1}s^{-2}$; thermal expansion coefficient, $\alpha = 4\times10^{-5}$ °C^{-1}.
1301
1302
1303

1304

	Analysis Method	Parameter	T_e = 30 km	T_e = 150 km
Flexure only	7.547-WT	T_e (km)	27.4 <u>27.4</u> 28.4	130.8 <u>140.8</u> 150.8
		F	0.49 <u>0.50</u> 0.50	0.48 <u>0.50</u> 0.53
	3.773-WT	T_e (km)	23.4 <u>23.4</u> 24.4	104.1 <u>116.1</u> 128.1
		F	0.49 <u>0.49</u> 0.50	0.44 <u>0.48</u> 0.51
	[1, 1]-MT	T_e (km)	26.0 <u>28.0</u> 30.0	95.7 <u>129.7</u> 158.7
		F	0.47 <u>0.49</u> 0.51	0.36 <u>0.47</u> 0.54
	[3, 4]-MT	T_e (km)	28.9 <u>28.9</u> 28.9	94.4 <u>102.4</u> 111.4
		F	0.51 <u>0.51</u> 0.51	0.40 <u>0.43</u> 0.46
R_{CG} = 1	7.547-WT	T_e (km)	26.4 <u>26.4</u> 27.4	78.9 <u>107.9</u> 133.9
		F	0.47 <u>0.48</u> 0.49	0.27 <u>0.40</u> 0.48
		η'	0.32 <u>0.34</u> 0.37	0.31 <u>0.34</u> 0.38
	3.773-WT	T_e (km)	20.0 <u>20.0</u> 20.0	61.3 <u>79.3</u> 101.3
		F	0.44 <u>0.44</u> 0.44	0.22 <u>0.33</u> 0.42
		η'	0.28 <u>0.32</u> 0.35	0.24 <u>0.32</u> 0.38
	[1, 1]-MT	T_e (km)	25.2 <u>27.2</u> 30.2	71.1 <u>126.1</u> 174.1
		F	0.45 <u>0.48</u> 0.51	0.22 <u>0.46</u> 0.57
		η'	0.22 <u>0.33</u> 0.41	0.18 <u>0.33</u> 0.47
	[3, 4]-MT	T_e (km)	26.2 <u>26.2</u> 26.2	55.8 <u>66.8</u> 78.8
		F	0.48 <u>0.48</u> 0.48	0.17 <u>0.25</u> 0.33
		η'	0.49 <u>0.51</u> 0.52	0.49 <u>0.52</u> 0.55
R_{CG} = 0	7.547-WT	T_e (km)	20.0 <u>21.0</u> 22.0	58.9 <u>77.9</u> 109.9

		F	0.38 <u>0.38</u> 0.40	0.01 <u>0.20</u> 0.36
		η'	0.12 <u>0.17</u> 0.22	0.05 <u>0.11</u> 0.17
	3.773-WT	T_e (km)	14.9 <u>14.9</u> 14.9	49.9 <u>58.9</u> 73.9
		F	0.31 <u>0.31</u> 0.31	0.01 <u>0.14</u> 0.25
		η'	0.28 <u>0.32</u> 0.37	0.01 <u>0.12</u> 0.22
	[1, 1]-MT	T_e (km)	19.4 <u>22.4</u> 26.4	53.2 <u>96.2</u> 158.2
		F	0.33 <u>0.39</u> 0.45	0.01 <u>0.30</u> 0.50
		η'	0.14 <u>0.32</u> 0.45	0.01 <u>0.15</u> 0.37
	[3, 4]-MT	T_e (km)	20.0 <u>21.0</u> 21.0	50.3 <u>56.3</u> 65.3
		F	0.38 <u>0.38</u> 0.38	0.01 <u>0.10</u> 0.18
		η'	0.40 <u>0.43</u> 0.46	0.15 <u>0.23</u> 0.29

Table 2. T_e, F, and η' results from inversion of the synthetic model admittances in Figure 5 (periodic data) using jackknifed error estimates. Values underlined are the best fitting estimates, and the values on either side show the lower and upper 95% confidence limits. Model parameters are $F = 0.5$ and $\eta' = 0.33$.

Analysis Method	Parameter	Region A	Region B
7.547-WT	T_e (km)	131.7 <u>158.7</u> 189.7	125.2 <u>158.2</u> 191.2
	F	0.46 <u>0.53</u> 0.59	0.46 <u>0.53</u> 0.58
	η'	0.21 <u>0.33</u> 0.45	0.01 <u>0.16</u> 0.33
	β	0.54 ± 0.14	0.32 ± 0.27
	$\bar{Q}_{O,0}$	65.81 ± 8.04	67.83 ± 16.72
5.336-WT	T_e (km)	118.0 <u>151.0</u> 185.0	145.3 <u>176.3</u> 214.3
	F	0.40 <u>0.51</u> 0.58	0.50 <u>0.56</u> 0.62
	η'	0.15 <u>0.30</u> 0.43	0.01 <u>0.18</u> 0.40
	β	0.50 ± 0.17	0.36 ± 0.30
	$\bar{Q}_{O,0}$	62.98 ± 9.07	66.82 ± 20.72

Table 3. T_e, F, and η' results from inversion of the observed admittances in North American regions A and B (Figures 6 and 7), using jackknifed error estimates. Values underlined are the best fitting estimates, and the values on either side show the lower and upper 95% confidence limits. In region A, the admittance profiles were inverted over the whole spectrum. In region B, the admittance profiles were inverted only using observations with wavelengths >800 km. Values of the fraction of the joint convective-GIA gravity anomaly due to GIA (β) and their errors were derived using equation (24), with their errors obtained from equation (25). Also shown are the mean long-wavelength observed admittance ($\bar{Q}_{O,0}$) and its error. The mean was calculated over the three longest wavelengths. The value of $\bar{Q}_{O,0}$

1322 that McKenzie [2010] observed (in region A) was 64 ± 5 mGal/km, and the T_e he recovered

1323 was 29 km.

1324

A_F	Parameter	T_e = 30 km	T_e = 150 km
1.6×10^{-6}	T_e (km)	26.9 <u>27.9</u> 28.9	119.4 <u>143.4</u> 166.4
	F	0.49 <u>0.50</u> 0.51	0.44 <u>0.51</u> 0.56
	η'	0.07 <u>0.10</u> 0.13	0.15 <u>0.19</u> 0.23
3.2×10^{-6}	T_e (km)	26.4 <u>26.4</u> 27.4	78.9 <u>107.9</u> 133.9
	F	0.47 <u>0.48</u> 0.49	0.27 <u>0.40</u> 0.48
	η'	0.32 <u>0.34</u> 0.37	0.31 <u>0.34</u> 0.38
6.4×10^{-6}	T_e (km)	24.7 <u>25.7</u> 25.7	61.4 <u>84.4</u> 114.4
	F	0.46 <u>0.47</u> 0.48	0.13 <u>0.29</u> 0.42
	η'	0.54 <u>0.56</u> 0.58	0.51 <u>0.54</u> 0.56

Table A1. T_e, F, and η' results from inversion of the $|\mathbf{k}_0|$ = 7.547 synthetic model admittances in Figures 5c and 5d, but with fixed A_F. The spectral amplitude of the flexural topography (A_F) in equation (43) was fixed at the three indicated values (3.2×10^{-6} is the value assumed in the main text), while maintaining ζ_F = 1.5, $T(k) = 2.7\times10^{-10}\ k^{-2}$, and a = 220 km, with other parameters given in Table 1. Jackknifed error estimates. Values underlined are the best fitting estimates, and the values on either side show the lower and upper 95% confidence limits. Model parameters are F = 0.5 and η' = 0.33.

A_F	Parameter	Region A
1.35×10^{-6}	T_e (km)	153.9 <u>181.9</u> 217.9
	F	0.49 <u>0.54</u> 0.55
	η'	0.11 <u>0.25</u> 0.40
2.7×10^{-6}	T_e (km)	131.7 <u>158.7</u> 189.7
	F	0.46 <u>0.53</u> 0.59
	η'	0.21 <u>0.33</u> 0.45
5.4×10^{-6}	T_e (km)	115.9 <u>142.9</u> 172.9
	F	0.41 <u>0.49</u> 0.56
	η'	0.42 <u>0.50</u> 0.59

Table A2. T_e, F, and η' results from inversion of the $|\mathbf{k}_0| = 7.547$ observed admittance in North American region A, but with fixed A_F. The spectral amplitude of the flexural topography (A_F) in equation (43) was fixed at the three indicated values (2.7×10^{-6} is the value assumed in the main text), while maintaining $\zeta_F = 1.5$, $T(k) = 8.0\times10^{-10}\ k^{-2}$, and $a = 220$ km, with other parameters given in Table 1. Jackknifed error estimates. Values in italics are the best fitting estimates, and the values on either side show the lower and upper 95% confidence limits.